Available online at www.sciencedirect.com
SCIENCE DIRECT
Journal of Sound and Vibration 293 (2006) 830–855
JOURNAL OF SOUND AND VIBRATION
www.elsevier.com/locate/jsvi

Three-dimensional train–track model for study of rail corrugation

X.S. Jin[a,*], Z.F. Wen[a], K.Y. Wang[a], Z.R. Zhou[a], Q.Y. Liu[a], C.H. Li[b]

[a]*State Key Laboratory of Traction Power, Southwest Jiaotong University, Chengdu 610031, China*
[b]*School of Civil Engineering, Southwest Jiaotong University, Chengdu 610031, China*

Accepted 26 August 2005
Available online 24 January 2006

Abstract

Rail corrugation is a main factor causing the vibration and noise from the structures of railway vehicles and tracks. A calculation model is put forward to analyse the effect of rail corrugation with different depths and wavelengths on the dynamical behaviour of a passenger car and a curved track in detail. Also the evolution of initial corrugation with different wavelengths is investigated. In the numerical analysis, Kalker's non-Hertzian rolling contact theory is modified and used to calculate the frictional work density on the contact area of the wheel and rail in rolling contact. The material loss per unit area is assumed to be proportional to the frictional work density to determine the wear depth of the contact surfaces of the curved rails. The combined influences of the corrugation development and the vertical and lateral coupled dynamics of the passenger car and the curved track are taken into account. The numerical results indicate that: (1) the corrugation with high passing frequencies has a great influence on the dynamical performance of the wheelset and track, but little on the carbody and the bogie frame; (2) the deeper the corrugation depth is, the greater the influence and the rail material wear are; but the longer the corrugation wavelength is, the smaller the influence and the wear are; and (3) the initial corrugation with a fixed wavelength on the rail running surface decreases with increasing number of the passenger car passages.

1. Introduction

When a train runs on a track with corrugated rails the structures of the train and track vibrate at large amplitude and generate much noise. Such a situation causes a reduction of the operational life of structural components, disturbs the living environment and reduces the comfort of the passengers. The phenomenon of rail corrugation has been observed and studied for over 100 years. According to a review of recently published papers on rail corrugation [1], their studies and the algorithms used include three main parts: (1) theoretical and numerical methods [2–17]; (2) experimental methods [18–20]; and (3) investigation and observation on site [21–27]. The studies with the theoretical and numerical methods involve a concept of feedback between the wear and the contact vibration of wheel and track [2–4], rolling contact theories with Hertzian form [5–8], high frequency structural vibrations of flexible wheelset and track or self-excited vibrations of them [9–11], plastic

*Corresponding author. Tel.: +86 28 87634355; fax: +86 28 87600868.
E-mail address: xsjin@home.swjtu.edu.cn (X.S. Jin).

0022-460X/$ - see front matter © 2006 Elsevier Ltd. All rights reserved.
doi:10.1016/j.jsv.2005.12.013

deformation theory of rail material [12], and non-Hertzian rolling contact theory for material wear calculation [13]. Refs. [13–16] put forward time-domain methods for the analysis of rail corrugation and dynamic coupling of train and track. The rail corrugation models in Refs. [13,14] considered the effect of the vertical dynamics of train and track, and the train–track models in Refs. [15,16] considered vertical and lateral coupled dynamics of the system. In Ref. [17], the influence of multiple wheel/rail interactions on rail corrugation was investigated. In Refs. [2–7], initial roughness profiles of rails with periodical variation are taken into account in their numerical calculations of rail corrugation. The latest corrugation experiments were carried out by Matsumoto et al. using a full-scale test facility [18,19]. In their experiments, a phenomenon of so-called "forced corrugation" was reproduced on the tread of the test wheelset since the high frequency excitation was applied to the rollers which simulated curved rails. In Ref. [20], corrugation was reproduced using a small-scale laboratory test stand.

In the present study, a calculation model is put forward to analyse the effect of rail corrugation with different depths and wavelengths on the dynamical behaviour of a passenger car and a curved track in detail. Also the evolution of initial corrugation with different wavelengths is investigated. In the numerical analysis, Kalker's non-Hertzian rolling contact theory is modified and used to calculate the frictional work density on the contact area of the wheel and rail in rolling contact. The material loss per unit area is assumed to be proportional to the frictional work density to determine the wear depth of the contact surfaces of the curved rails. The combined influences of the corrugation and the vertical and lateral coupling dynamics of the passenger car and the curved track are taken into consideration. For simplicity, the numerical model of corrugation calculation considers a half-passenger car with a two-axle bogie and a double-suspension system, and a simplified curved track, in which an Euler beam is used to model the rails, the structural components under the rails are replaced with equivalent springs, dampers and masses. The undulatory wear on the running surfaces of the rails, passed by the four wheels of the same bogie, is calculated simultaneously.

2. Calculation model for corrugation

2.1. Model of passenger car and track

Corrugation occurring on curved tracks are the most serious at railway sites. In the present calculation a curved track with radius $R_0 = 300$ m and a half-passenger car are selected. A transition curve with length 80 m is followed by a circular curve of length 100 m. The track gauge is 1437 mm. The sleeper spacing is 600 mm. The super-elevation of the outside rail of the track is 100 mm, the rail inclination is 1/40, and the type of rails laid has mass 60 kg/m. The half-passenger car is equipped with a bogie with two wheelsets and double suspension systems. The nominal rolling radius of the wheelsets with worn profile is $r_0 = 457.5$ mm. The curving speed of the passenger car is 80 km/h. Since the half-passenger car is considered in the analysis of dynamic performance of the vehicle coupled with the curved track, it cannot be balanced when it is running on the track. Therefore, the pitching and yaw motions of the carriage have to be neglected. These pitching and yaw vibrations of the carriage have low frequencies; usually ranging from 1 to 2 Hz, so such vibrations have little influence on rail corrugation with wavelength less than 2 m. The calculation model of the half-passenger car and the track is shown in Figs. 1(a) and (b). The left and right wheels of the leading wheelset are denoted as wheel 1 and 2 and the corresponding wheels of the trailing wheelset are denoted as wheel 3 and 4. In Fig. 1, Z with different subscripts indicates the vertical displacement of the parts of the passenger car and the track, Y denotes the lateral displacement, θ indicates the pitching angle, ϕ indicates the rolling angle, P_{wrzk} ($k = 1, 2, 3, 4$) indicate the vertical loads between the four wheels and the rails, C and K with subscripts stand for the coefficients of the equivalent dampers and the stiffness coefficients of the equivalent springs, respectively. The equivalent dampers and springs are used to replace the connections between the components of the passenger car and the track, as shown in Fig. 1. Since the system contains many differential equations and the detailed derivation of the equations is tedious, the equations are given directly, and their symbols are explained in the following text.

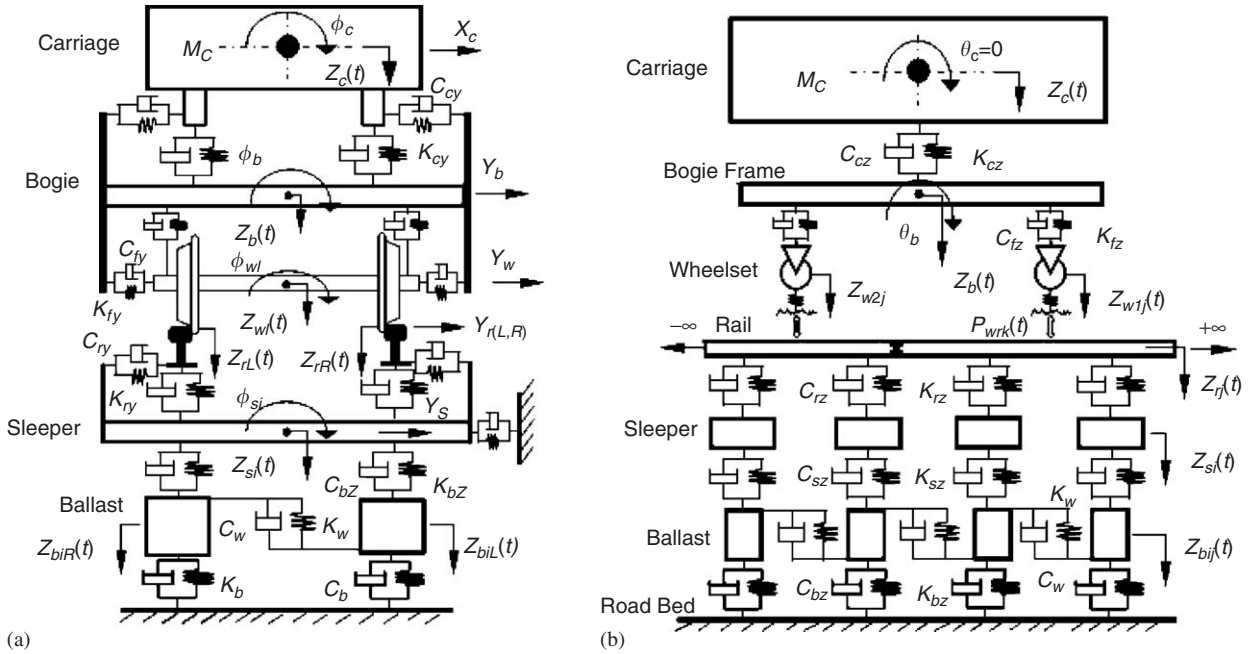

Fig. 1. (a) Elevation of a half-passenger car coupled with a curved track: (b) side elevation.

2.1.1. Equations of passenger car system

The vertical, lateral and roll differential equations of the half-carriage are:

$$M_c\left[\ddot{Z}_c - a_0\ddot{\phi}_{\sec} + \frac{v^2}{R_c}\phi_{\sec}\right] = -F_{ztL} - F_{ztR} + M_c g, \tag{1}$$

$$M_c\left[\ddot{Y}_c + \frac{v^2}{R_c} + H_{rc}\ddot{\phi}_{\sec}\right] = F_{ytL} + F_{ytR} + M_c g\phi_{\sec}, \tag{2}$$

$$I_{cx}[\ddot{\phi}_c + \ddot{\phi}_{\sec}] = -(F_{ytL} + F_{ytR})H_{cB} + (F_{ztL} - F_{ztR})d_s, \tag{3}$$

where M_c is the mass of the half-carriage, $\ddot{Z}_c$ and $\ddot{Y}_c$ are the vertical and lateral accelerations of the half-carriage centre, $\ddot{\phi}_c$ is the roll angular acceleration, $\phi_{\sec}$ and $\ddot{\phi}_{\sec}$ are the angular deflection and angular acceleration of the carriage rolling caused by the super-elevation of the outside rail, v is the curving speed, H_{rc} is the height of the carriage centre from the contact point of wheel and rail when the train is static on centre line of the curved track, a_0 is the half-distance between the nominal rolling circles of a wheelset, R_c is the instantaneous radius of the curved track at the centre of the carriage, g is the gravity acceleration, $F_{ztL}(F_{ztR})$ and $F_{ytL}(F_{ytR})$ are, respectively, the vertical and lateral forces between the carriage and the bogie frame, subscripts L and R indicate the left and right sides of the carriage, respectively, I_{cx} is the moment of inertia of the half-carriage in roll, H_{cB} is the height of the half-carriage centre from the secondary suspension location (C_{cz} and K_{cz}), as shown in Fig. 1, and d_s is the half-distance between the secondary suspension systems of the two sides of the bogie. The yaw, pitch and longitudinal motions of the carriage body are ignored.

The equations of motion of the bogie in the vertical, lateral, roll, pitch and yaw directions are:

$$M_t\left[\ddot{Z}_t - a_0\ddot{\phi}_{\sec t} + \frac{v^2}{R_t}\phi_{\sec t}\right] = F_{ztL} - F_{zfL1} - F_{zfL2} + F_{ztR} - F_{zfR1} - F_{zfR2} + M_t g, \tag{4}$$

$$M_t[\ddot{Y}_t + v^2/R_t + (r_0 + H_{tw})\ddot{\phi}_{\sec t}] = -F_{ytL} + F_{yfL1} + F_{yfL2} - F_{ytR} + F_{yfR1} + F_{yfR2} + M_t g\phi_{\sec t}, \tag{5}$$

$$I_{tx}[\ddot{\phi}_t + \ddot{\phi}_{set}] = -[F_{yfL1} + F_{yfR1} + F_{yfL2} + F_{yfR2}]H_{tw} + [F_{zfL1} + F_{zfL2} - F_{zfR1} - F_{zfR2}]d_w + (F_{ztR} - F_{ztL})d_s - (F_{ytL} + F_{ytR})H_{Bt}, \quad (6)$$

$$I_{ty}\ddot{\beta}_t = [F_{zfL1} + F_{zfR1} - F_{zfL2} - F_{zfR2}]l_t - [F_{xfL1} + F_{xfR1} + F_{xfL2} + F_{xfR2}]H_{tw}, \quad (7)$$

$$I_{tz}[\ddot{\psi}_t + vd(R_t^{-1})/\mathrm{d}t] = [F_{yfL1} + F_{yfR1} - F_{yfL2} - F_{yfR2}]l_t + [F_{xfR1} + F_{xfR2} - F_{xfL1} - F_{xfL2}]d_w, \quad (8)$$

where M_t is the mass of the bogie, $\ddot{Z}_t$ and $\ddot{Y}_t$ are the vertical and lateral accelerations of the bogie centre, $\ddot{\phi}_t$, $\ddot{\beta}_t$ and $\ddot{\psi}_t$ are the angular accelerations of the bogie in roll, pitch and yaw, H_{tw} is the height of the bogie centre from the wheelset centre, H_{Bt} is the height of the secondary suspension from the bogie centre, d_w is the half-distance between the two primary suspensions of the two sides of the bogie, l_t is the half-distance between the two axles of the bogie, R_t is the instantaneous radius of the curved track at the centre of the bogie, ϕ_{set} and $\ddot{\phi}_{set}$ are the angular deflection and angular acceleration of the bogie in roll caused by the super-elevation of the outside rail, I_{tx}, I_{ty} and I_{tz} are the moments of inertia of the bogie in pitch, roll and yaw, $F_{zfLi}(F_{zfRi})$, $F_{yfLi}(F_{yfRi})$ and $F_{xfLi}(F_{xfRi})$ are the forces in the vertical, lateral and longitudinal directions of the primary suspensions of the bogie, subscripts L and R indicate the left and right sides, $i = 1, 2$ indicate the front and rear primary suspensions, the primary suspension systems, indicated by C_{fZ} and K_{fz} in Fig. 1, are used to support the bogie frame and set on the two wheelsets. In Eq. (8) $vd(R_t^{-1})/\mathrm{d}t$ stands for the influence of the curvature radius variation of the curved track on the yaw motion of the bogie when the passenger car is passing through the transition curve. The longitudinal motion of the bogie centre is neglected, namely, it is assumed that the acceleration of the bogie centre in the rolling direction equals zero.

The equations of motion of wheelset i ($i = 1, 2$) in the vertical, lateral, roll, yaw and pitch directions are:

$$M_w\left(\ddot{Z}_{wi} - a_0\ddot{\phi}_{sewi} - \frac{v^2}{R_{wi}}\phi_{sewi}\right) = (F_{zfLi} + F_{zfRi}) + M_w g - \sum_{j=1,2} F_{wrzj}, \quad (9)$$

$$M_w(\ddot{Y}_{wi} + v^2/R_{wi} + r_0\ddot{\phi}_{sewi}) = (-F_{yfLi} - F_{yfRi}) + M_w g\phi_{sewi} + \sum_{j=1,2} F_{wryj}, \quad (10)$$

$$I_{wx}(\ddot{\phi}_{sewi} + \ddot{\phi}_{wi}) - I_{wy}(\dot{\beta}_{wi} - v/r_0)(\dot{\psi}_{wi} + v/R_{wi}) = a_0(F_{wrz1} - F_{wrz2}) - r_{L1}F_{wry1} - r_{R1}F_{wry2} + d_w(F_{zfRi} - F_{zfLi}), \quad (11)$$

$$I_{wz}[\ddot{\psi}_{wi} + vd(R_{wi}^{-1})/\mathrm{d}t] - I_{wy}(\dot{\phi}_{sew1} + \dot{\phi}_{wi})(\dot{\beta}_{wi} - v/r_0) = a_0(F_{wrx1} - F_{wrx2}) + a_0\psi_{wi}(F_{wry1} - F_{wry2}) + M_{wrz1} + M_{wrz2} + d_w(F_{xfLi} - F_{xfRi}), \quad (12)$$

$$I_{wy}\ddot{\beta}_{wi} = r_{R1}F_{wrx1} + r_{L1}F_{wrx2} + r_{R1}\psi_{w1}F_{wry2} + r_{L1}\psi_{w1}F_{wry1} + M_{wry1} + M_{wry2}, \quad (13)$$

where M_w is the mass of the wheelset, $\ddot{Z}_{wi}$ and $\ddot{Y}_{wi}$ are the vertical and lateral accelerations of wheelset i, $\ddot{\phi}_{wi}$, $\ddot{\beta}_{wi}$ and $\ddot{\psi}_{wi}$ are the angular accelerations in roll, pitch and yaw, r_{Li} and r_{Ri} are, respectively, the left and right instant rolling circles of wheelset i, R_{wi} is the instantaneous radius of the curved track at the centre of the wheelset, ϕ_{sewi} and $\ddot{\phi}_{sewi}$ are the angular deflection and angular acceleration of the wheelset in roll caused by the super-elevation of the outside rail, I_{wx}, I_{wy} and I_{wz} are the moments of inertia of the wheelset in pitch, roll and yaw, F_{wrxj}, F_{wryj} and F_{wrzj} ($j = 1, 2$) are the forces between the wheels and rails in X, Y and Z directions, $j = 1, 2$ indicate wheels 1 and 2, $M_{wrz1}(M_{wzy1})$ and $M_{wrz2}(M_{wry2})$ are the spin moment components between the high rail and wheel 1, and the low rail and wheel 2, respectively, subscripts z and y indicate the vertical and lateral directions. In Eqs. (11) and (12), $vd(R_{wi}^{-1})/\mathrm{d}t$ stands for the influence of the curvature radius variation of the curved track on the yaw motion of the wheelset, and $I_{wy}(\dot{\beta}_{wi} - v/r_0)(\dot{\psi}_{wi} + v/R_{wi})$ and $I_{wy}(\dot{\phi}_{sewi} + \dot{\phi}_{wi})(\dot{\beta}_{wi} - v/r_0)$ indicate the interferences between the wheelset curving and rotating, and the curving and roll, respectively. It is obvious that an interaction of the left and right wheels of the same bogie on the left and right rails is considered in the rail corrugation calculation. However, the longitudinal acceleration of the wheelset centre is assumed always to be zero, and the flexible deformation of the wheelset is also neglected.

2.1.2. Equations of curved track system

The calculation model of the track used in Ref. [28] is introduced in the present paper. Due to the half-passenger car passing through the curved track, the four wheels of the same bogie interact with the two rails. Each rail is modelled by an Euler beam. The calculation length of the rails is 12 m. The two ends of the calculation rails are hinged. The vertical and lateral bending deformations and twisting of the rails are taken into account. The longitudinal deformation and the cross influence of the vertical and lateral bending and twisting deformations of the rails are ignored. Using the Rayleigh–Ritz method the fourth-order partial differential equations of the rail are converted into second-order ordinary equations as follows:

$$\ddot{q}_{zk}(t)+\frac{EI_y}{m_r}\left(\frac{k\pi}{l}\right)^4 q_{zk}(t)=-\sum_{i=1}^{N}F_{zi}Z_k(x_{si})+\sum_{j=1,3\ or\ 2,4}F_{wrzj}Z_k(x_{wj})\quad (k=1\sim NMZ), \tag{14}$$

$$\ddot{q}_{yk}(t)+\frac{EI_Z}{m_r}\left(\frac{k\pi}{l}\right)^4 q_{yk}(t)=-\sum_{i=1}^{N}F_{yi}Y_k(x_{si})+\sum_{j=1,3\ or\ 2,4}F_{wryj}Y_k(x_{wj})\quad (k=1\sim NMY), \tag{15}$$

$$\ddot{q}_{Tk}(t)+\frac{GK}{\rho I_0}\left(\frac{k\pi}{l}\right)^2 q_{Tk}(t)=-\sum_{i=1}^{N}M_{si}\Theta_k(x_{si})+\sum_{j=1,3\ or\ 2,4}M_{wj}\Theta_k(x_{wj})\quad (k=1\sim NMT). \tag{16}$$

Eqs. (14), (15) and (16) are, respectively, the vertical, lateral and torsional equations of motion. $q_{zk}(t), q_{yk}(t)$ and $q_{Tk}(t)$ are the generalized coordinates, and describe the vertical, lateral and torsional motions of the rail, EI_y, EI_z and GK are the vertical bending, lateral bending and torsional stiffness of the rail, m_r is the mass per unit longitudinal length, I_0 is the radial second moment of area of the rail, ρ is the density of the rail material, $Z_k(\cdots)$, $Y_k(\cdots)$ and $\Theta_k(\cdots)$ are the kth mode functions of the rail in vertical bending, lateral bending, and torsion, x_{si} $(i=1,2,\ldots,N)$ are the coordinates of the sleepers, and x_{wj} $(j=1,3$ or $2,4)$ are the coordinates of the contact points of the wheel and rail. $NMZ=NMY=NMT=100$, which is the total numbers of the rail mode functions selected in the calculation. The sleeper pitch equals 0.6 m, $N=20$, which denotes the total number of sleeper spans, and so the calculation length of rail $l=0.6\times 20$ m is 12 m. F_{zi} and F_{yi} are, respectively, the vertical and lateral supporting forces of the rail due to sleeper i. F_{wrzj} and F_{wryj} are the vertical and lateral forces between wheel j and corresponding rail. It is noted that Eqs. (14)–(16) with subscript $j=1,3$ or $2,4$ stand for the equations of the left and right rails, respectively. From Eqs. (14) to (16), it is obvious that an interaction of the two axles of the bogie on the rails is taken into account. In Eq. (16), M_{si} and M_{wj} are the equivalent calculated moments on the rail, as shown in Fig. 2 for the right rail. Fig. 2 illustrates the rail force diagram corresponding to the rail fastening system. According to Fig. 2, F_{zi}, M_{si} and M_{wj} in Eqs. (14)–(16) are written as

$$\begin{aligned} F_{zi}&=F_{z1i}+F_{z2i},\\ M_{si}&=(F_{z2i}-F_{z1i})b-F_{yi}a\quad (i=1,2,\ldots,N),\\ M_{wj}&=F_{wryj}h_R-F_{wrzj}e\quad (j=1,3\text{ or }2,4). \end{aligned} \tag{17}$$

In Fig. 2, e is the distance from the vertical load point of the wheel/rail contact point to the central line of the rail, O_r is the twisting centre of the rail, a, b and h_R are indicated in Fig. 2. In Eq. (17), subscripts $j=1,3$ stand for wheels 1, 3 running on the left rail, and $j=2,4$ stand for wheels 2, 4 on the right rail. It should be noted that the formulae expressing F_{z1i}, F_{z2i} and F_{yi} include the deflections of the rail and sleeper, and the coefficients of the equivalent spring stiffness and damper of the rail fastening system. They are omitted for brevity. Through the dynamic calculation, $q_{zk}(t), q_{yk}(t)$ and $q_{Tk}(t)$ $(k=1,2,3,\ldots,NMZ$ (or NMY or $NMT))$ are obtained. Therefore, the vertical, lateral and torsional displacements of the rail are written as

$$Z_r(x,t)=\sum_{k=1}^{NMZ}Z_k(x)q_{zk}(t),\quad Y_r(x,t)=\sum_{k=1}^{NMY}Y_k(x)q_{yk}(t),\quad \phi_r(x,t)=\sum_{k=1}^{NMT}\Theta_k(x)q_{Tk}(t). \tag{18}$$

Sleeper i $(i=1,2,\ldots,20)$ is represented by a rigid rectangular beam in the calculation model, as shown in Fig. 3. In Fig. 3, $F_{ziL}, F_{yiL}, F_{ziR}$ and F_{yiR} are the forces between the sleeper i and the left and right rails, F_{ysbi} is

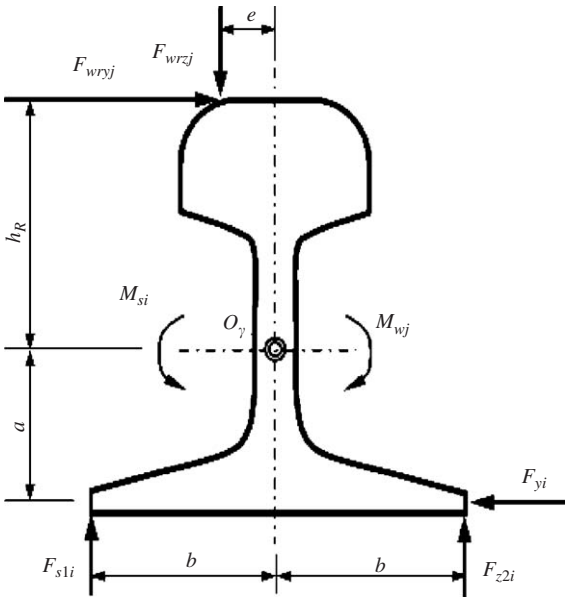

Fig. 2. Rail force diagram.

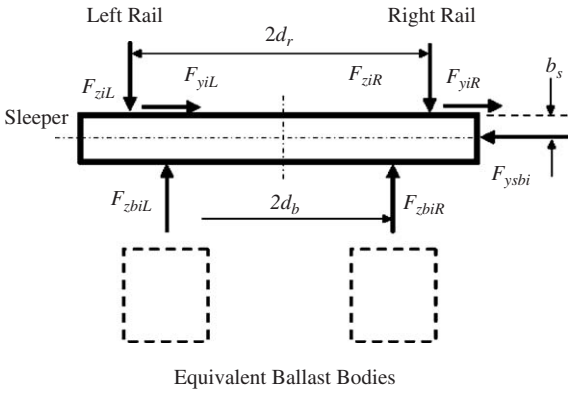

Fig. 3. Sleeper force diagram.

the equivalent support force due to the ballast in the lateral direction (see Fig. 1(b)), F_{zbiL} and F_{zbiR} are the vertical support forces due to the equivalent ballast bodies, d_r is the half-distance between the left and right rails, d_b is the half-distance between the centres of the left and right ballast bodies. In the dynamic analysis the vertical, lateral and roll motions of sleeper i are considered simultaneously.

The ballast bed is replaced with the equivalent rigid ballast bodies, as shown in the left side of Fig. 4. Considering equivalent ballast bodies A and B, their calculation model is shown in the right side of Fig. 4. In Fig. 4, $F_{zfiL}, F_{zriL}, F_{zfiR}, F_{zriR}$ and F_{ziLR} are the vertical shear forces between the neighbouring ballast bodies, F_{zgiL} and F_{zgiR} are the vertical forces between the ballast bodies and the road-bed (ground). In the dynamic analysis, only the vertical motion of centres of the ballast bodies is taken into account.

For brevity, the differential equations of the sleeper and the ballast bodies are omitted in the paper. It is noted that the mathematical expressions of the force parameters in Figs. 3 and 4 include the displacements and the corresponding velocity of the sleeper and the ballast bodies, the stiffness coefficients of the equivalent springs, and damping coefficients of the equivalent dampers at the corresponding positions, as shown in Fig. 1. The mathematical expressions are straightforward but tedious.

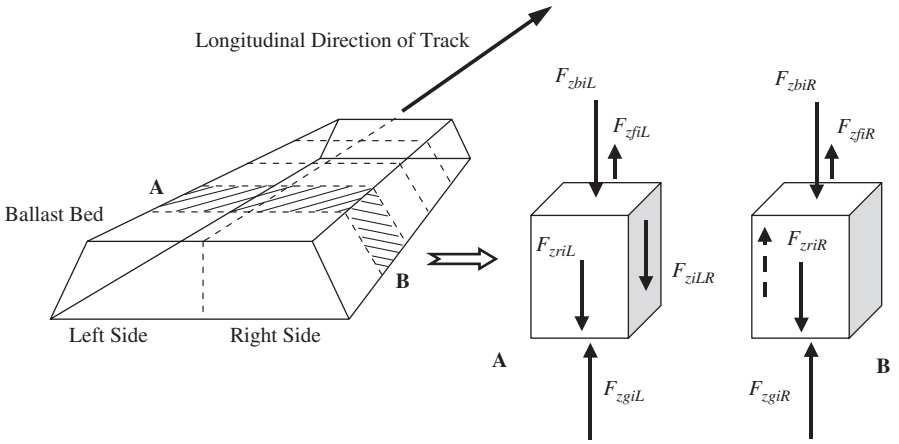

Fig. 4. Force diagram of equivalent ballast bodies.

2.1.3. Model of wheel–rail contact

In the analysis of the transient coupling dynamics of the passenger car and the curved track, it is necessary that an accurate and quick calculation model of coupling of the wheel–rail system is used. The calculation model of wheel–rail coupling, usually, includes the normal and tangential contact problems. Considering the influence of the undulatory wear of the rail running surface on the normal load, the usual model of the wheel–rail normal load reads

$$P_{wrnj}(t) = \begin{cases} C_H[Z_{wnj} - Z_{rnj} + \delta_0 - U_{wj}]^{3/2}, & Z_{wnj} - Z_{rnj} + \delta_0 - U_{wj} > 0, \\ 0, & Z_{wnj} - Z_{rnj} + \delta_0 - U_{wj} \leqslant 0, \end{cases} \tag{19}$$

where $j = 1,\ 2,\ 3$ and 4 indicate wheels 1, 2, 3 and 4, respectively, Z_{wnj} and Z_{rnj} are the normal displacements of wheel j and the rail at their contact point, and they are determined by solving Eqs. (1)–(19) and calculating the contact geometry of the wheelset and the rails. δ_0 is the approach between the wheel and rail caused by the static normal load when the passenger car is on the central line of the tangent track. U_{wj} is the depth of the undulatory wear on the rail running surface, at the contact point of wheel j and the rail. It should be noted that the model of the normal contact load Eq. (19) is approximately described with a Hertzian contact spring with a unilateral restraint. In Eq. (19), $Z_{wnk} - Z_{rnk} + \delta_0 - U_w > 0$ indicates the wheel–rail in contact, and $Z_{wnk} - Z_{rnk} + \delta_0 - U_w < 0$ stands for separation. C_H is the coefficient of the normal contact stiffness concerning the Hertzian contact condition of the wheel and rail, selected as $1.13 \times 10^{11}\mathrm{N/m^{3/2}}$ [28].

Shen–Hedrick–Elkins' model is adopted as the calculation model of the tangential force between the wheel and rail [29]. The components, $F_{\tau xj}$ and $F_{\tau yj}$, of the instantaneous tangential force, and spin moment M_{wrnj} are easily and quickly calculated by using the model of Shen et al. the known instantaneous normal load and the known instantaneous creepages. $F_{\tau xj}$ and $F_{\tau yj}$ denote the tangential force components in the longitudinal and lateral directions, respectively. If P_{wrnj}, $F_{\tau yj}$ and M_{wrnj} are obtained at any time instant, $F_{wrzj}, F_{wrzj}, M_{wrzj}$ and M_{wrzj} in the above concerned equations are expressed in terms of $P_{wrnj}, F_{\tau yj}$ and M_{wrn}. They read

$$\begin{aligned} F_{wrzj} &= P_{wrnj}\cos\delta_j + F_{\tau yj}\sin\delta_j, \\ F_{wryj} &= -P_{wrnj}\sin\delta_j + F_{\tau yj}\cos\delta_j, \\ M_{wrzj} &= M_{wrnj}\cos\delta_j, \\ M_{wryj} &= -M_{wrnj}\sin\delta_j. \end{aligned} \tag{20}$$

Eqs. (20) are based on Fig. 5. In Fig. 5, vectors $\mathbf{n}$ and $\boldsymbol{\tau}$ denote, respectively, the normal and tangential directions of the wheel and the rail at their contact point. δ_j indicates the contact angle of wheel j and the rail.

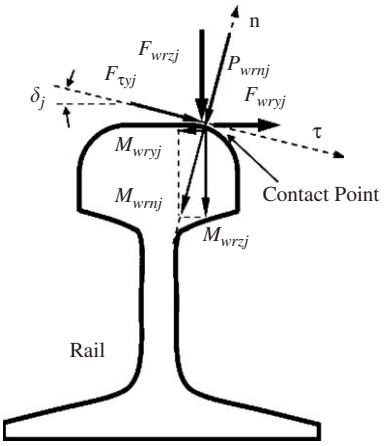

Fig. 5. Forces at contact point of rail.

2.1.4. Initial and boundary conditions of track system

The two ends of the Euler beams modelling the rails are hinged, namely the deflections and bending moments at the beam ends are zero. The deflection of the road bed is neglected; only the vertical deflections of the equivalent ballast bodies are taken into account. The boundary conditions of the equivalent ballast bodies read

$$Z_{bL0} = \dot{Z}_{bL0} = 0, \quad Z_{bL(N+1)} = \dot{Z}_{bL(N+1)} = 0,$$
$$Z_{bR0} = \dot{Z}_{bR0} = 0, \quad Z_{bR(N+1)} = \dot{Z}_{bR(N+1)} = 0. \tag{21}$$

Eq. (21) indicate that the vertical deflections and velocities of the equivalent ballast bodies at the two ends of the track considered are zero.

Zhai [30] developed a numerical method specifically to solve the coupled dynamic equations of the railway vehicle and track. The stability, calculation speed and accuracy of the numerical method for solving Eqs. (1)–(21) were also discussed in detail.

2.1.5. Dynamic characteristics of passenger car and track

Considering the influence of the equivalent springs and dampers of the track on the occurrence of corrugation, their values are given and listed in Table 1. In Table 1 subscripts y, z stand for the lateral and vertical directions; r, s and b stand for the equivalent springs and dampers between the rails and the sleepers (railpad), the sleepers and the ballast mass body, and the ballast mass body and the roadbed, respectively; subscript w stands for the equivalent vertical shear springs and dampers between the two equivalent mass bodies of the ballast in the vertical direction. The other parameter values of the passenger car and the track are listed in Table 2 [31].

The resonance frequencies and the modes of the track play an important role in wavelength formation of rail corrugation [2]. For the above prescribed model of the vehicle and track and the parameters listed in Table 1, an investigation into the natural modes and resonance frequencies of the track, in the vertical and lateral directions, respectively, is carried out with the commercial finite element code ANSYS 8.0. In the analysis the rails are still modelled with Euler beams. The calculation length of the rail covers 35 sleeper spans. Through the detailed analysis it is found that the rail calculation length has little influence on the results concerning the natural frequencies and modes of the track when it covers 35–70 sleeper spans. The natural frequencies found range from 0 to 2000 Hz. The two ends of the rail are hinged. In such a situation, the deflections and bending moments at the beam ends are zero. Since the calculation length of the curved track covers only 35 sleeper spans, the effect of the track curvature on the structural modes is ignored in the modal analysis. Thus, the track is assumed to be symmetrical about the central and vertical plane of the track. In the modal analysis, it is found that the vertical and lateral modal frequencies are quite different, and the parallel

Table 1
Coefficients of equivalent springs and dampers

K_{ry}/C_{ry}	K_{rz}/C_{rz}	K_{sy}/C_{sy}	K_{sz}/C_{sz}	K_w/C_w	K_{bz}/C_{bz}
2.947×10^7 N/m	7.8×10^7 N/m	3.0×10^7 N/m	7.0×10^7 N/m	7.8×10^7 N/m	6.5×10^7 N/m
5.0×10^4 Ns/m	5.0×10^4 Ns/m	6.0×10^4 Ns/m	6.0×10^4 Ns/m	8.0×10^4 Ns/m	3.1×10^4 Ns/m

Table 2
Parameters of structures of passenger car and track

Parameter	Value	Parameter	Value	Parameter	Value
M_c (kg)	1.7×10^4	K_{fy} (MN/m)	5	M_s (kg)	349
M_t (kg)	3.0×10^3	K_{fz} (MN/m)	0.55	M_b (kg/m)	466
M_w (kg)	1.4×10^3	C_{cy} (kN s/m)	60	E (N/m^2)	2.1×10^{11}
I_{cx} (kg m^2)	3.8×10^4	C_{cz} (kN s/m)	80	I_y (m^4)	3.217×10^{-5}
I_{tx} (kg m^2)	2.26×10^3	C_{fz}(kN s/m)	6	I_z(m^4)	5.24×10^{-6}
I_{ty} (kg m^2)	2.71×10^3	d_w (m)	0.978	I_0 (m^4)	3.741×10^{-5}
I_{tz} (kg m^2)	3.16×10^3	d_s (m)	1.21	ρ (kg/m^3)	7.8×10^3
I_{wx} (kg m^2)	915	l_t (m)	1.2	GK (N m/rad)	1.9587×10^5
I_{wy} (kg m^2)	140	a_0 (m)	0.7465	$H_L \cdot H_R$ (m)	0.09453
I_{wz} (kg m^2)	915	r_0 (m)	0.4575	a (m)	0.08147
K_{cx} (MN/m)	0.15	H_{cB} (m)	1.145	b (m)	0.075
K_{cy} (MN/m)	0.15	H_{Bt} (m)	−0.081	d_r(m)	0.755
K_{cz} (MN/m)	0.4	H_{tw} (m)	0.14	l_s (m)	2.5
K_{fx} (MN/m)	10	m_r (kg/m)	60.64	L_s (m)	0.6

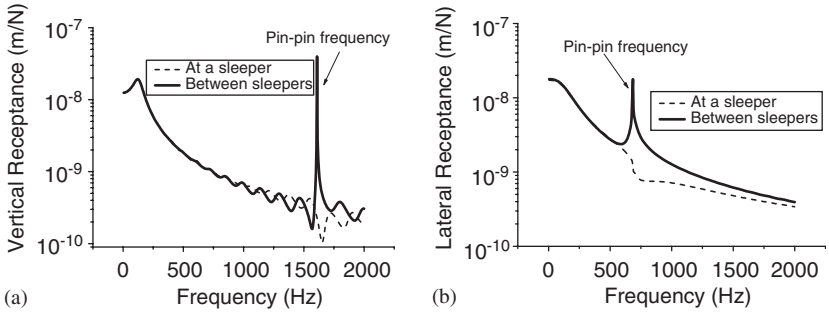

Fig. 6. (a) Vertical receptance of the track; (b) lateral receptance of the track.

rails of the track have symmetrical, anti-symmetrical and unsymmetrical modes about the central and vertical plane of the track. It is also found that the first 10 resonance frequencies, especially for the lateral direction, are very close to each other. The interval between the neighbouring resonance frequencies gradually increases with increasing frequency.

By applying a harmonic load with different frequencies to different positions in a sleeper span of the track in the vertical and lateral directions the receptance for different positions of the sleeper span was obtained. Figs. 6(a) and (b) illustrate the vertical and lateral receptance of the track.

The receptance of the track represents the dynamic flexibility of the rail but its usefulness in interpreting the results of rail corrugation is limited. A smaller flexibility (or larger track stiffness) leads to a larger normal load

between the wheel and rail, and greater material wear on the rail running surface [2–5]. However, in a coupled wheel/rail system, variations in the flexibility of the track, due to discrete sleeper supports, cause an excitation of the system, and the varying normal load is a response to the system. The phases of the excitation and the response, along rail running surface, are different. Therefore, the maximum normal load does not occur at the rail position above the sleeper where the stiffness is the largest. The most serious wear of the rail material does not form above the sleeper. The position where the most serious wear occurs depends on the sleeper span and the rolling speed of wheel [32]. At the pinned–pinned frequency, the track vibration causes large wear of the rail above the sleeper. However, the track vibration at the pinned–pinned frequency may not be excited as a wheelset passes over the track as the frequency range of the system response depends greatly on the frequency range and the energy of the excitation to the system. Therefore, the initiation and growth of rail corrugation cannot be clearly described according to the dynamic properties of the track in the frequency domain. The coupled dynamic behaviour of wheel and rail have to be considered in the time domain during the wheelset passage. In addition, the interaction of the four wheels (leading and trailing wheelsets) cannot be ignored in the rail corrugation calculation. The authors found the differences between the results obtained by two time-domain corrugation models. One model only considered the coupled dynamic behaviour of a single wheel and the track [32], and the other considers the interactions of four wheels of the same bogie in the present paper. The undulatory wear patterns caused by the four wheels of the same bogie are very different.

In the range from 0 to 2000 Hz, the track has many resonance frequencies. It is difficult to decide which frequencies play a key role in the initiation and growth of the corrugation. The wheelset rolling speed and the track natural frequencies easily excited have a great influence on the rail corrugation wavelength. The frequencies of the track vibration depend on the energy and frequency range of excitation of the track. Actually, the excitations between the wheels and the rails are variable. They are caused by the irregularities of the track and wheels.

In order to clarify the track natural frequencies that are excited during the wheelset passages, a half-sine with length 30 mm and depth 0.01 mm is selected to model a dent on the high (outer) rail head in the vertical and lateral directions, respectively, and used as an irregular input to the system of the half-passenger car and the track. Through the dynamic simulation using the vehicle-track model discussed above, the fluctuating normal loads of the wheel and rail are obtained. Their linear spectra show the main vibration frequencies, as shown in Fig. 7. Fig. 7(a) illustrates the linear spectrum of the normal load fluctuation caused by the dent on the rail head in the lateral direction, and Fig. 7(b) indicates that caused by the vertical dent. It is obvious that two main frequencies of the system vibration, $f_A \approx 40$ and $f_B \approx 740$ Hz, are easily excited when the passenger car passes the track. These two frequencies dominate the wavelengths or passing frequencies of the corrugation development. From the above modal analysis it is known that f_A is not a resonance frequency of the track. It corresponds approximately to the sleeper passing frequency of the track which is about 37 Hz, obtained by dividing the train speed of 22.2 m/s by the sleeper span. Probably, f_A should be attributed to the discrete sleeper supports. This frequency will be further investigated in detail. If the assumed dent is placed on the low rail, peaks occur at the same frequencies when the passenger car passes over the dent.

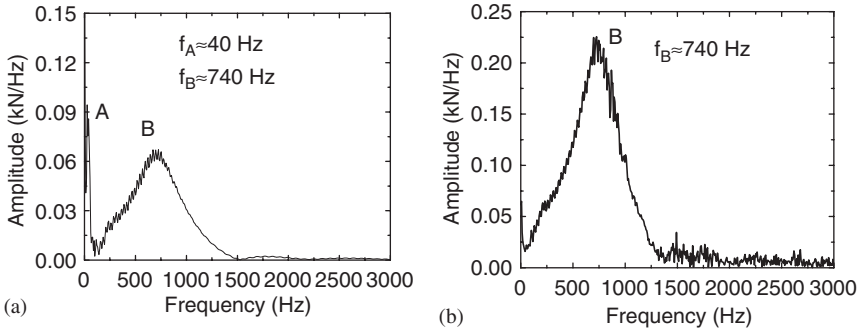

Fig. 7. (a) Linear spectrum of normal load fluctuation caused by a lateral dent; (b) caused by a vertical dent.

2.2. Wear calculation of rail running surface

2.2.1. Calculation of tangential traction and slip on contact patch

FASTSIM [33] and Kalker's rolling contact theory of three-dimensional elastic bodies [34] are available for the calculation of tangential traction and slip on the contact patch of wheel–rail with elastic deformation. However, FASTSIM was developed based on Hertzian assumptions, one of which is that the radii of curvature of the elastic bodies in contact are constant near their contact point. If geometry irregularities or undulatory wear with small wavelengths exist on the rail running surface, this assumption is broken. If so, it is difficult to determine the radii of curvature prior to calculating the flexibility coefficients of the contacting bodies in using FASTSIM for repeated wear calculation of the rail material. If the initial values of the radii of curvature were always used in the repeated wear calculation, it could lead to large cumulative errors in the material wear and profile change of the rail.

It is therefore very desirable to use Kalker's non-Hertzian rolling contact theory of three-dimensional elastic bodies in the analysis of rolling contact of wheel and rail with geometry irregularities or undulatory wear with small wavelengths. This is because the rolling contact theory model does not include the radii of curvature of the contacting bodies at their contact point. It is described in detail in Chapter 4 of Ref. [34]. The computer code CONTACT includes several modules for rolling contact calculation. One of them implements the numerical calculation of Kalker's rolling contact theory with non-Hertzian form. However, this module in CONTACT cannot be directly used in repeated calculation of wheel–rail rolling contact if the continuous profile change of the rail, due to wear, is considered. Therefore, the module needs to be modified a little. To that end, w_{30} is defined as the depth of the initial irregularity profile at the contact point on the rail. $w_{3J}^{(m)}$ is the new undulatory accumulated wear depth at the same contact point after m wheel rolling passages. It is assumed that all the wear takes place only on the rail surface. Considering the influence of w_{30} and $w_{3J}^{(m)}$ on the normal distance between the wheel and rail (as shown in Fig. 8(a)), the discrete form of the principle of complementary virtual work of the wheel and corrugated rail in rolling contact is written as follows:

$$\begin{aligned} \min\ C &= \tfrac{1}{2}p_{Ii}A_{IiJj}p_{Jj} + \{[(h_J + w_{30} + w_{3J}^{(m)} - h_{\min}) - q]p_{J3} + (W_{J\tau} - u'_{J\tau})p_{J\tau}\}A_0 \\ \text{s.t.}:\quad & p_{J3} \geqslant 0, |p_{J\tau}| \leqslant b_J, \\ & A_0 \sum_{J=1}^{M} p_{J3} = P_{wrnk}, \quad \forall \mathbf{x} \in A_c. \end{aligned} \tag{22}$$

In Eq. (22) subscripts $i = 1, 2, 3$ stand for the directions of the x_1, x_2 and x_3 axes (see Fig. 8), $\tau = 1, 2$ denote the directions of x_1 and x_2, I, J are the numbers of the rectangular elements in Fig. 8(b). A_{IiJj} is the influence coefficient of force/displacement, indicating the i direction displacement occurring at the centre of rectangular element I caused by the j direction unit force acting at the centre of rectangular element J. p_{iI} is the component of traction on element I. h_J is the value of the normal gap h (shown in Fig. 8(a)) at the centre of element J, which is obtained by the calculation of contact geometry of the wheel/rail mentioned above. q is the unknown approach in the direction of x_3. $u'_{J\tau}$ is the component of the elastic difference of the pair of contact particles at

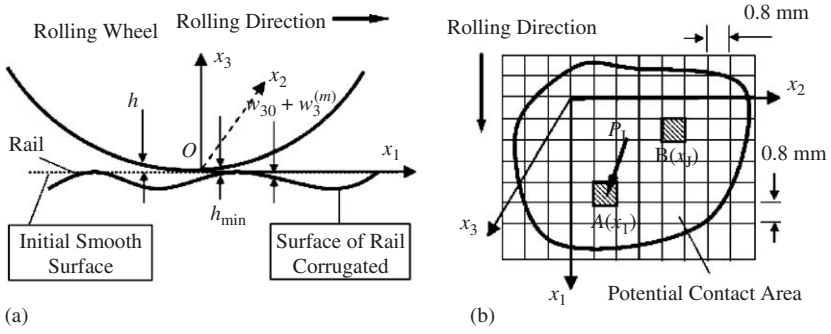

Fig. 8. (a) Description of normal distance variation; (b) mesh covering a potential contact area.

centre of element J at the previous time step t', $A_0 = \Delta x_1 \times \Delta x_2 = 0.8 \times 0.8 = 0.64\,\text{mm}^2$, which is the area of the rectangular element, A_C is the potential contact area, M is the total number of the rectangular elements, selected as $21 \times 21 = 441$ in the calculation. b_J is the bound of Coulomb friction at the centre of element J, which reads

$$\begin{aligned} b_J &= fp_{J3} \quad \mathbf{x} \in H, \\ b_J &= f'p_{J3} \quad \mathbf{x} \in S, \end{aligned} \tag{23}$$

where f, f' are the static and kinetic Coulomb friction coefficients, selected as $f = f' = 0.3$. H and S are, respectively, the stick and slip areas in the contact area.

In Eq. (22), P_{wrnk} ($k = 1, 2, 3$ and 4), the total normal load, is obtained through the calculation of the coupling dynamics of the vehicle and curved track discussed in Section 2.1. $W_{J\tau}$ ($\tau = 1, 2$) is the component of the rigid slip between the wheel and rail at the centre of element J from the previous time step t' to the present time step t, and written as

$$W_{J\tau} = \int_{t'}^{t} [\xi_{\tau k} + (-1)^{\tau} x_{3-\tau} \xi_{3k}] v_0 \, \mathrm{d}\varsigma \quad (\tau = 1, 2,\ k = 1, 2, 3, 4). \tag{24}$$

In Eq. (24) $\xi_{\tau k}$ are the creepages of the wheel and rail, also obtained through the dynamics calculation, subscript $\tau = 1, 2$ and 3 indicate the longitudinal, lateral and spin creepages of the wheel and rail, and $k = 1, 2, 3$ and 4 indicate wheels 1, 2, 3, and 4. It is noted that the creepages indicate the slips between the wheel and rail, at their contact point, which are caused by the wheel and rail rigid motion and the rail structure deformation. The rail structure deformation indicates its bending and twisting deformations, instead of the local elastic deformation in or near the contact area of the rail. x_1 and x_2 are the coordinates of the centre of element J, v_0 is the speed of the wheel rolling, t' and t are the previous time step and the present time step in the continuous calculation.

The mathematical programming method is used to find the solution to Eq. (22) [34]. Therefore, $p_{Ji}, u'_{J\tau}$ ($i = 1, 2, 3, \tau = 1, 2, J = 1, 2, \ldots, 441$) in Eq. (22) are obtained. The Poisson's ratio and shear modulus of the material used in the calculation are 0.3 and $7.8125 \times 10^4\,\text{N/mm}^2$.

2.2.2. Material wear model of wheel and rail

The material wear model in which material loss mass per unit area is proportional to frictional work of unit area reads [6,14,15,35,36]

$$\Delta m(x_1, x_2) = C_w f_w(x_1, x_2). \tag{25}$$

In Eq. (25), $\Delta m(x_1, x_2)$ is the material mass loss per unit area at point (x_1, x_2), $C_w = 1.0 \times 10^{-9}\,\text{kgNm}$ [6,14,15] which is the wear coefficient, and $f_w(x_1, x_2)$ the frictional work density. Considering the square element I in the contact area, as shown in Fig. 8(b), and the results obtained with the above rolling contact theory, Eq. (25) is rewritten as

$$\Delta m(x_{I1}, x_{I2}) = C_w f_w(x_{I1}, x_{I2}) = C_w |S_{I1} p_{I1} + S_{I2} p_{I2}|, \tag{26}$$

where $S_{I\tau}$ is the component of the total slip of the wheel and rail at the centre of element I in the direction of x_τ, given by

$$S_{I\tau} = W_{I\tau} + p_{J\tau'} A_{J\tau' I\tau} - u'_{I\tau} \quad (\tau, \tau' = 1, 2,\ I, J = 1, 2, \ldots, 441). \tag{27}$$

In Eq. (27), $W_{I\tau}$ is calculated with Eq. (24), $p_{J\tau'} A_{J\tau' I\tau} - u'_{I\tau}$ stands for the component of the local elastic deformation difference at the centre of element J (see Fig. 8(b)), at the present time step t. It is should be noted that the subscripts τ' and J in Eq. (27) are summed over their ranges.

Considering the first passage of the passenger car, for instance, the depth of wear at the centre of element I is written as

$$w_{I3}^{(1)} = C_w |S_{I\tau} p_{I\tau}| / \rho \quad (\tau = 1, 2), \tag{28}$$

where $\rho = 7.8 \times 10^3\,\text{kg/m}^3$, which is the density of the rail material. After k passages the total wear depth is the sum of each wear depth.

The above calculation model of rail corrugation is described simply by Fig. 9. h_k is the normal distance between wheel k and the rail. $k = 1, 2, 3$ and 4 denote wheels 1, 2, 3 and 4, respectively. ξ_{jk}, P_{wrnk}, Y_{wi}, ψ_{wi} and Y_{rk} are obtained through the dynamics calculation of the passenger car and track. h_k and δ_k are obtained through the contact geometry calculation of the wheelset and the track. ξ_{jk}, P_{zk}, h_k and δ_k are used in the calculation of the traction and slip on the contact patch of the wheel and rail (see Eqs. (22) and (23)). The frictional work density f_{wk} on the contact patch is determined. If the frictional work density is known, the wear depth on the running surface is determined with the material wear model at the present step (see Eq. (28)). Before the next loop calculation is carried out, the profiles of the rails need to be modified, due to the new wear. Using the accumulated material wear on the rail running surface, the maximum depth of the undulatory wear along the rail running surface is determined, and then used as an input of rail irregularity to the system of the half-passenger car and the curved track, for the next step calculation of the dynamics. Fig. 9 indicates a feedback process between the transient coupling dynamics of the passenger car and the curved track and long-term wear processes.

The calculation length of rail corrugation considered along the rail running surface is selected to be only 3.2 m. It is 90 m from the location of the calculated corrugation to the connection between the tangent track and the entering transition curve, as shown in Fig. 10. For each passage of the passenger car, the calculation length of the dynamics covers the entire curved track.

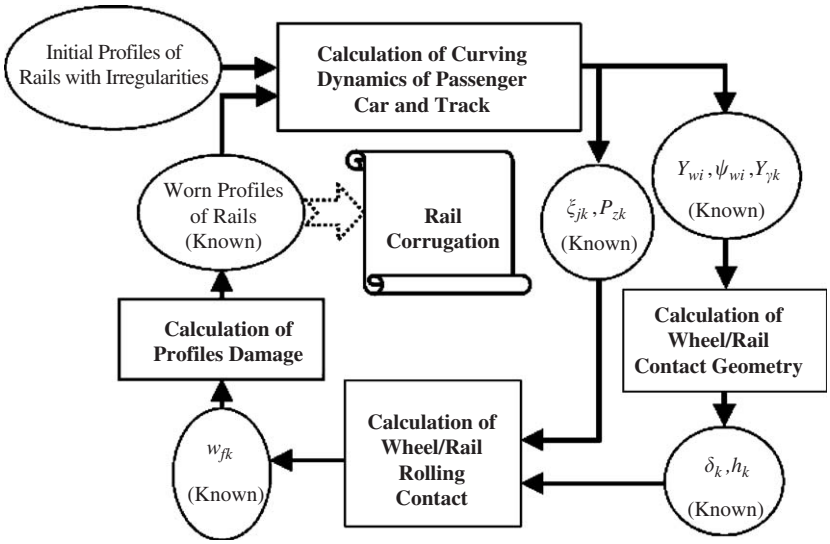

Fig. 9. Description of the calculation model of rail corrugation.

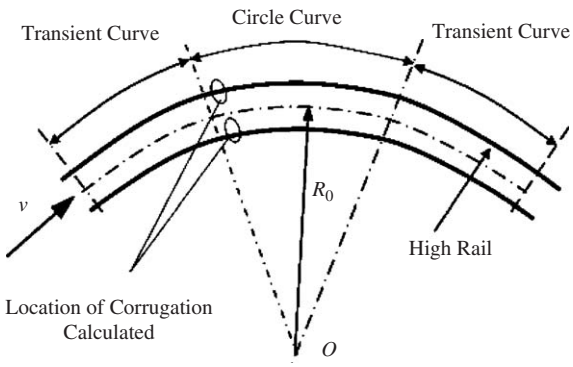

Fig. 10. Location of corrugation calculated on the curved track.

3. Numerical results and discussions

3.1. Effects of corrugation with different depths and wavelengths

Usually, the rail corrugation present in the railway field reveals different depths of undulatory wear and various different passing frequencies or wavelengths. Their depth and wavelength have a great influence on the dynamic performance of the vehicle and the track and the new wear on the rail running surface. Such influence is investigated with the present numerical method. To that end, it is assumed that an initial corrugation has different depths and same wavelength, or different wavelengths and same depth. Considering the different positions of the leading and trailing wheelsets in the longitudinal direction of the track, the depths of the initial corrugation under the leading and trailing wheelsets are described by

$$W_{\mathrm{CL}} = d_p\left[1-\cos\left(\frac{2\pi(x+l_b)}{\lambda}\right)\right], \quad W_{\mathrm{CT}} = d_p\left[1-\cos\left(\frac{2\pi x}{\lambda}\right)\right]. \tag{29}$$

In Eq. (29), W_{CL} indicates the maximum wave-depth of the corrugation at the contact point of the leading wheelset and the rails, W_{CT} corresponds to that under the trailing wheelset, x is the distance of the wheelset rolling along the entire curved track, d_p is the depth, λ is the wavelength, and $l_b = 2.4$ m, which is the distance between the leading and trailing wheelsets. The cosine irregularity described by Eq. (29) is placed on the entire curved track. It is noted that first and second formulae denote the same applied irregularity on the curved rails. Eq. (29) expresses the initial assumed corrugation depths at the two different contact points.

When the passenger car passes through the curved track at speed 80 km/h with the initial corrugation with wavelength of 30 mm and depths $2d_p$ of 0.002, 0.01 and 0.05 mm, the dynamic performance of the vehicle and the track changes very much, and also the behaviour of the wheels/rails vary periodically. Fig. 11 illustrates the fluctuations of the normal load between the high rail and wheel 1. Under an excitation of the initial corrugation with a depth of 0.05 mm, the amplitude of the normal load fluctuation increases to about two time of the quasi-static normal load which is 56 kN. The wavelength of fluctuation is the same as that of the initial corrugation. Fig. 12 indicates the fluctuations of the normal loads between the rails and the four wheels of the same bogie under an excitation of the corrugation of 0.01 mm depth. The normal load fluctuation of the outside wheel/rail is larger than that of the inside wheel/rail.

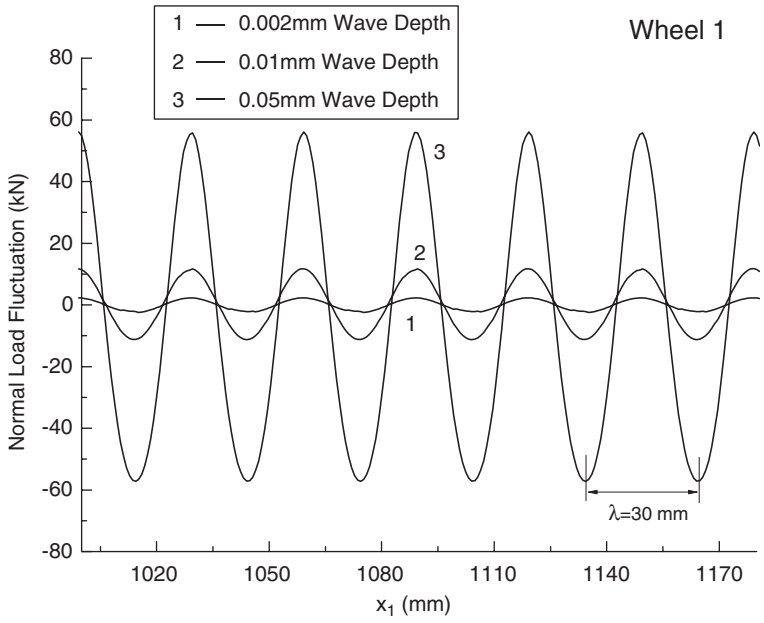

Fig. 11. Normal load of wheel 1 and the rail.

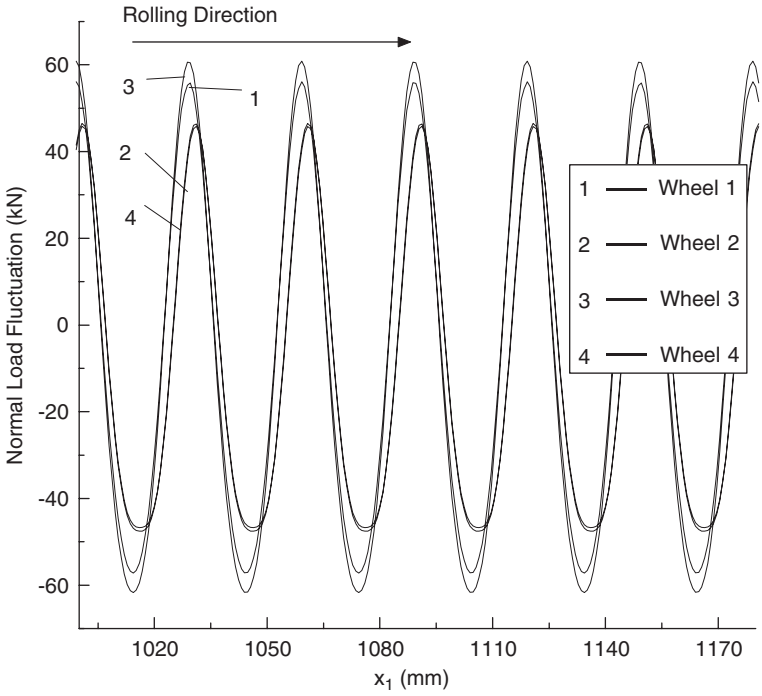

Fig. 12. Normal load of 4 wheels and rails.

Such a situation causes a greater undulatory material wear on the outside rail than on the low (inner) rail of the curved track. From Fig. 12, the phases of the fluctuations of the normal loads have a little difference since an interaction of the leading wheelset and the rails affects that of the trailing wheelset and the rails. Therefore, the phases of the new corrugation caused by the four wheels of the same bogie are different. Due to the corrugation excitation, the creepages, stick/slip areas of the wheels and rails vary with the same frequency as that of the normal load fluctuation. Fig. 13 illustrates the creepages of wheels 1, 3 under an excitation of the corrugation with 0.01 mm wave-depth. Curves 1–3 indicate the lateral, longitudinal and spin creepages. The thick lines denote the creepages of wheel 1, and thin broken lines denote those of wheel 3. It is clear that the absolute values of the lateral and longitudinal creepages of the leading wheelset are much larger than those of the trailing wheelset, and also the oscillation amplitude of the creepage is larger than that of the trailing wheelset. The constant and undulatory wear caused by the leading wheelset are, of course, much greater than those caused by the trailing wheelset. But there is little difference between their spin creepages. The wavelength or frequency of the creepage oscillation is the same as that of the corrugation excitation or the normal load. In Fig. 13, the lateral creepages and the longitudinal creepage of wheel 3 are constant over the distance 150 mm shown. Actually, the creepages change from zero to the values present in Fig. 13 as the passenger car moves from the tangent track to the location of the calculated corrugation, as shown in Fig. 10. The lateral creepage of wheel 1, indicated by thick line 2, oscillates with a small amplitude and 30 mm wavelength. The step-like behaviour of the spin creepages is due to quantization errors in the output. Between wheels 2, 4 and the low rail, the almost same situation occurs as that between wheels 1, 3 and the high rail.

When the train passes through the circular curve of the curved track, the yaw angles of the leading and trailing wheelsets are about 0.31° and -0.076°, and their lateral shifts are about 10 and 4.7 mm, respectively. The contact areas of the leading wheelset and the rails get into a full slip situation. However, a stick area exists in the contact areas of the trailing wheelset and the rails. The contact areas and stick/slip areas vary periodically along the running surfaces of the rails. Figs. 14 and 15 illustrate the variations of the stick/slip areas, normal loads and frictional works of the high rail and wheels 1 and 3, respectively, under an excitation of the corrugation with 0.01 mm depth. The larger normal load causes the larger stick/slip areas and frictional work, and also causes deeper wear on the rail running surface according to Eqs. (25)–(28). Fig. 14 shows that

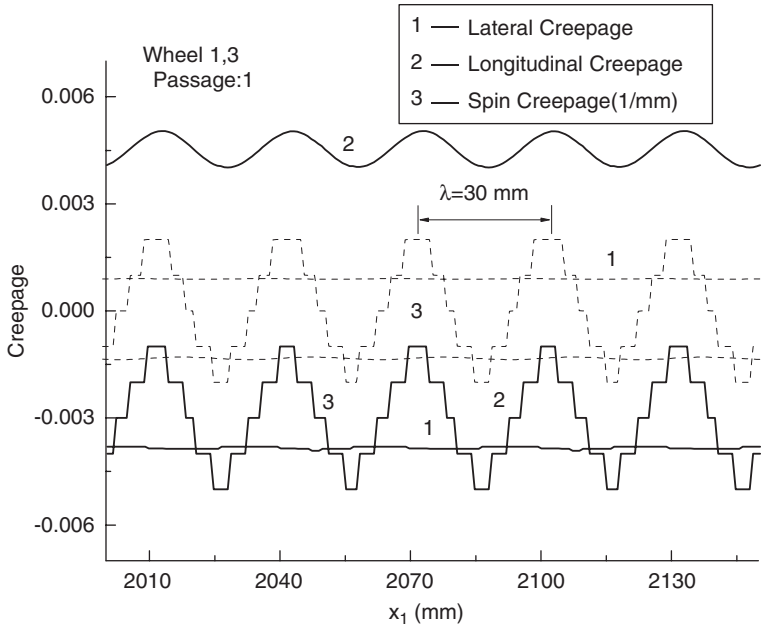

Fig. 13. Creepages between wheels 1, 3 and high rail.

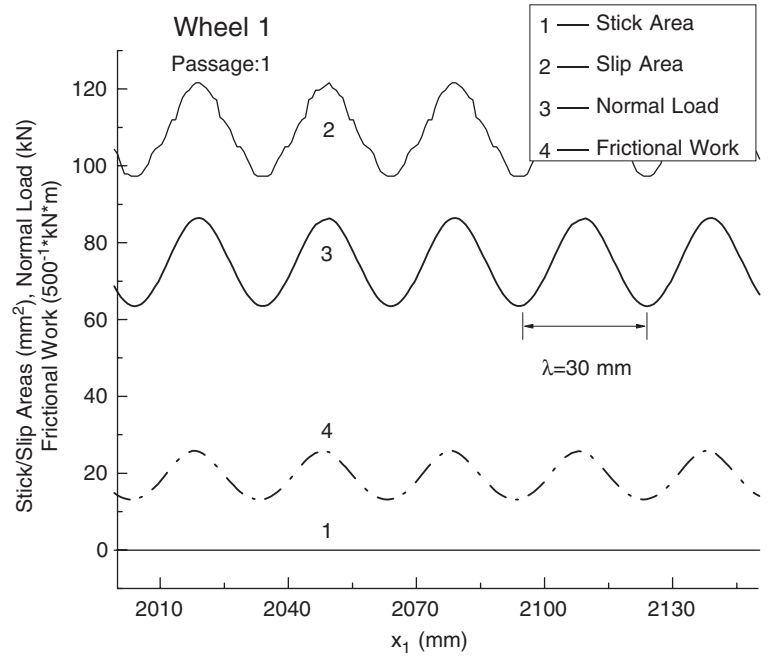

Fig. 14. Stick/slip areas, normal load and frictional work.

the stick area vanishes in the contact patch of wheel 1 and the high rail. The same situation occurs in the contact patch of the low rail and wheel 2 (namely the right wheel of the leading wheelset). But the contact area of the high rail and wheel 3 includes a stick area, which is about one-third of the whole contact area. It should be noted that the contact area is the sum of its stick and slip areas.

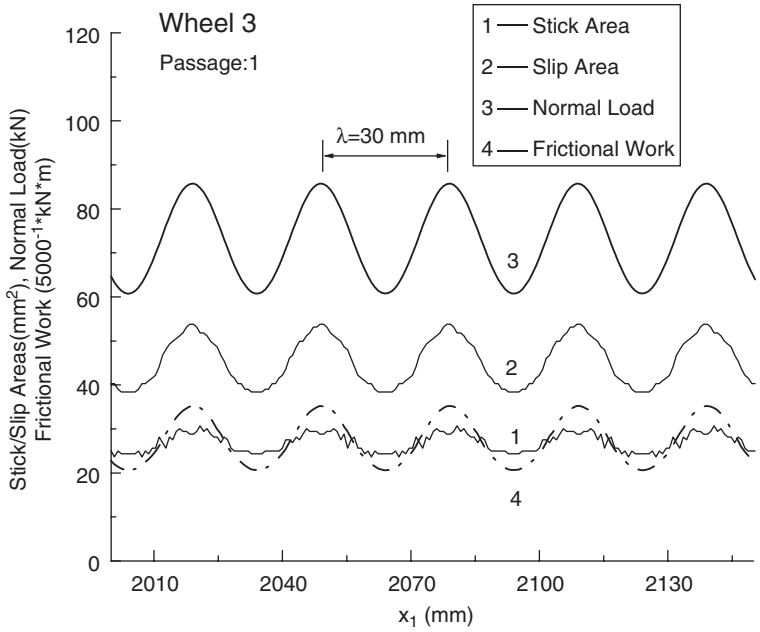

Fig. 15. Stick/slip areas, normal load and frictional work.

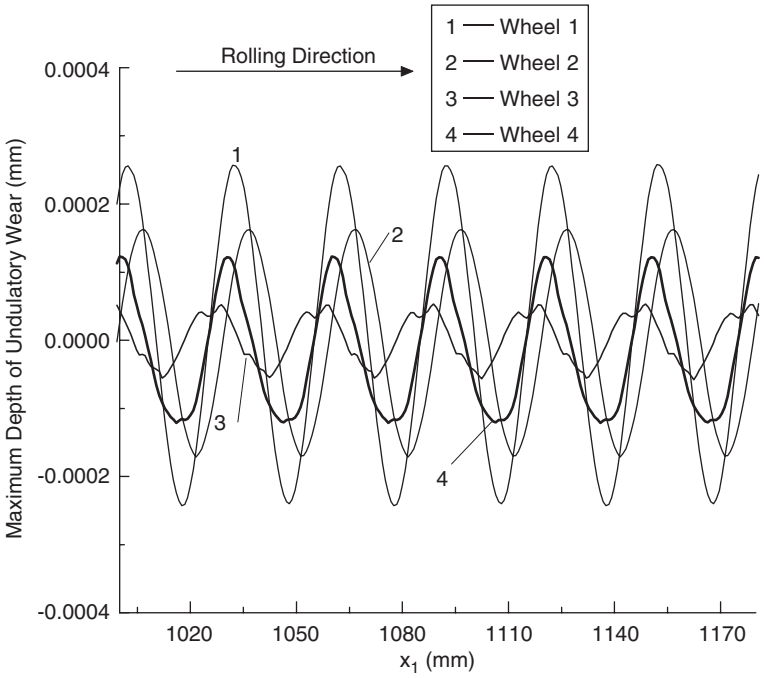

Fig. 16. Maximum wave-depth of undulatory wears caused by 4 wheels.

When the passenger car passes through the curved rails corrugated with 0.01 mm depth the new undulatory wear forms on the running surfaces of the rails passed by the four wheels of the same bogie. Fig. 16 illustrates the maximum depth variations of the new undulatory wear. The maximum wave-depth caused by the leading wheelset is as about two times that caused by the trailing wheelset. Although the phases of the initial

corrugation excitation to the four wheels are assumed to be same, the phases of the new undulatory wears caused by them are different due to the interactions of the four wheels of the same bogie. Their wavelength is the same as that of the initial corrugation.

Fig. 17 illustrates the patterns of new wear caused by an excitation of the corrugation with 30 mm wavelength and 0.002, 0.01 and 0.05 mm depths. The figures in the left column indicate the new wears occur on the high rail running surface passed by wheel 1, and those in the right column indicate the situation caused by wheel 3. The patterns present the constant wears and the wave wears on the rail running surfaces passed by the wheels after the first passage of the passenger car. The wavelength of the new wave wear is the same as that of the initial corrugation. Fig. 17(b) shows only mild wave wear since the initial corrugation excitation with 0.002 mm depth causes the small fluctuation of the normal loads, as shown in Fig. 11. However, the depth of the new wave wear increases quickly with an increase of the initial corrugation depth. From Fig. 12, the fluctuating amplitudes of the normal loads of wheels 1 and 3 are almost the same under the same initial

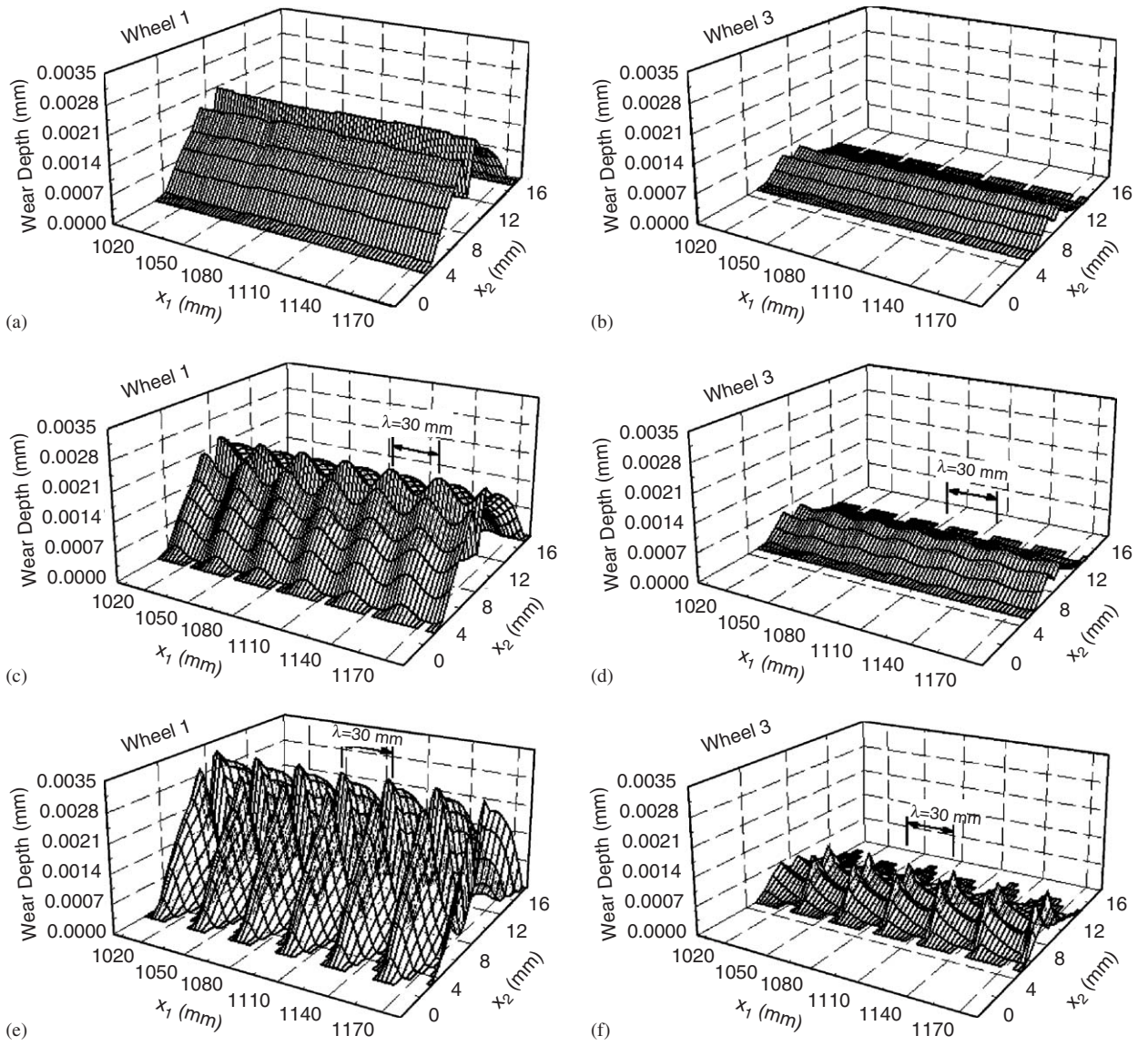

Fig. 17. Patterns of new wear caused by excitation of corrugation with different depths: (a) and (b) under excitation of 0.002 mm depth corrugation; (c) and (d) under excitation of 0.01 mm depth corrugation; (e) and (f) under excitation of 0.05 mm depth corrugation.

Table 3
Acceleration of wheelset and track structure parts

Excitation amplitude	Item	W-l (g)	W-t (g)	R-1 (g)	R-2 (g)	R-3 (g)	R-4 (g)	Slp (g)	Bal-L (g)	Bal-R (g)
0.002 mm	Ac./V	0.634	0.671	6.454	5.616	6.847	5.744	0.8	0.0249	0.229
	Ac./L	0.059	0.063	2.293	1.275	0.766	0.469	0.033		
0.01 mm	Ac./V	3.142	3.309	31.37	28.216	34.082	28.559	4.025	0.12	0.115
	Ac./L	0.147	0.317	10.792	6.383	3.793	2.33	0.166		
0.05 mm	Ac./V	14.523	15.482	155.20	132.80	168.96	134.55	18.806	0.624	0.504
	Acc/L	1.188	1.935	49.55	29.02	22.67	13.94	0.731		

Letters V, L indicate the vertical and lateral directions, W-l and W-t stand for the leading and trailing wheelsets, R-1, R-2, R-3 and R-4 stand for the contact points under wheels 1, 2, 3 and 4, Slp stands for the sleeper close the leading wheelset, and Bal-L and Bal-R stand for the left and right equivalent ballast mass body. The accelerations are given in terms of gravitational acceleration $g = 9.81\,m/s^2$. The amplitudes listed are measured from peak to trough.

corrugation excitation. But the depth and width of the wear caused by wheel 1 are much larger than those caused by wheel 3. This is because the creepages of wheel 1 and their fluctuating amplitudes are much larger than those of wheel 3, as shown in Fig. 13. According to Eqs. (24)–(28), the creepages are the key factors to determine the wear. The occurrence of larger creepages on wheel 1 is due to the larger attack angle and lateral deflection of the leading wheelset. Therefore, under an excitation of the same irregularity, the undulatory rail wear caused by the leading wheelset is much more serious than that caused by the trailing wheelset of the bogie when the passenger car passes through the curved track.

Through the analysis, it is found that the rail corrugation with high passing frequencies affects the dynamic performance of the bogie and the carriage of the passenger car little, but affects that of the wheelset and track structure very much. Table 3 indicates the maximum oscillation amplitudes of the vertical and lateral accelerations of the centres of the wheelsets and the track parts under the excitation of the corrugation with different depths. The oscillation frequency of the accelerations is the same as that of the corrugation excitation.

In railway track, existing corrugation presents different wave-depths, and also presents a few different wavelengths. In the present paper, the effect of the corrugation excitation with 0.01 mm depth, and 30, 80 and 200 mm wavelengths, on the dynamic performance is investigated. When the passenger car passes through the curved rails corrugated with 30, 80 and 200 mm wavelength, the vibration amplitudes of the structures of the passenger car and the track are much different. If the wavelength of the corrugation excitation increases, the fluctuation amplitudes of the normal load, the acceleration and the creepage decrease very much. For instance, under an excitation of the corrugation with 200 mm wavelength, the amplitude of the wheelset centre acceleration oscillation is about 1/10 of that under the corrugation excitation with 30 mm wavelength. So the depth of the new undulatory wear caused by the corrugation with larger wavelength (or lower passing frequency) is smaller than that caused by the corrugation with smaller wavelength (higher passing frequency). According to dynamics theory, this conclusion is easily understood. At a constant running speed, the rail corrugation with deeper wave-depth and higher passing frequency has the larger energy of excitation to the coupled system of railway vehicle and track. Therefore, such rail corrugation excitation causes a greater vibration of the system, the large creepages and normal loads between the rails and the wheels, and the serious undulatory wear on the running surfaces of the rails.

3.2. Development of initial corrugation with increasing number of wheel passages

Some published papers have a discussion on the development of the initial corrugation existing on the rail with increasing number of train passages. One of their conclusions is that if the passing frequency of the initial corrugation is the same as the natural frequency of the track, the wheel/rail system resonance occurs. The initial corrugation develops fast. This phenomenon is further investigated with the present numerical method. To that end, an initial corrugation with 30 mm wavelength and 0.005 mm wave-depth is assumed to exist on

the curved rails. It is described with the following functions:

$$C_L = d_p\left[1-\sin\left(\frac{2\pi(x+l_b)}{\lambda}\right)\right]\left[1-\sin\left(\frac{2\pi y}{\lambda_y}\right)\right],\quad C_T = d_p\left[1-\sin\left(\frac{2\pi x}{\lambda}\right)\right]\left[1-\sin\left(\frac{2\pi y}{\lambda_y}\right)\right]. \tag{30}$$

In Eq. (30), the first formula denotes the initial corrugation passed by the leading wheelset, the second passed by the trailing wheelset, $d_p = 0.00125$ mm, $\lambda = 30$ mm, λ_y is the width of the initial corrugation in the lateral direction, y is the coordinate of the rail running surface in the lateral direction, $l_b = 2.4$ m, the distance from the leading wheelset to the trailing wheelset. It is noted that C_L and C_T indicate the same initial corrugation placed on all the curved rails considered. At the positions of the leading and the trailing wheelsets the initial corrugation mathematical expression has a longitudinal distance difference l_b, as described by Eq. (30). If the passenger car passes through the curved rails with the initial corrugation at 80 km/h, the passing frequency of the initial corrugation is 740.7 Hz, which is obtained by dividing the running speed, 80 km/h, by 30 mm wavelength. This frequency approximately equals the track resonance frequency f_B, as shown in Fig. 8.

After 1, 10 and 30 passages of the passenger car, the evolutions of the initial corrugation caused by wheel 1 are illustrated with Figs. 18(a), (b) and (c), respectively. It is obvious that the depth of the corrugation from peak to trough gradually becomes shallow with increasing number of passenger car passages. The main

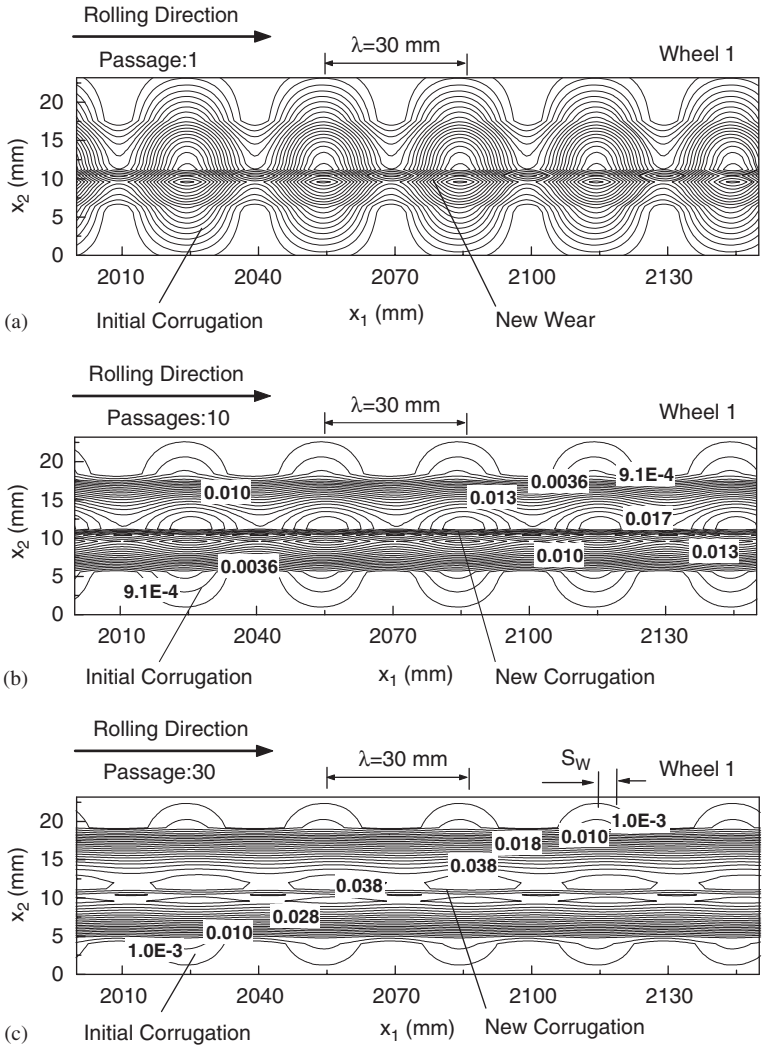

Fig. 18. Patterns of initial corrugation evolution: (a) 1 passage; (b) 10 passages; (c) 30 passages.

wavelength of the initial corrugation evolution is the same as that of the initial corrugation. Almost the same situation occurs on the running surfaces of the rails passed by the other 3 wheels of the same bogie. In Fig. 18 the new corrugation has a tendency to move forward. After 30 passages, the new corrugation surpasses the initial corrugation for $S_w \approx 4$ mm, as shown in Fig. 18(c). Fig. 19 indicates the maximum depth variation of the new corrugation corresponding to Fig. 18. The above explanation for Fig. 18 is further clarified according to Fig. 19. It is noted that Fig. 19 shows the new undulatory wear without the constant wear, namely, the constant wear is taken off. Due to the decrease of wave-depth of the initial corrugation with increasing number of passages, the vibration amplitudes of the normal loads, creepages, and the accelerations of the wheels and the rails decrease gradually. Fig. 20 illustrates the normal load variation of wheel 1 and the high rail after 1, 10, 20 and 30 passages of the passenger car. After 30 passages, the oscillation amplitude of the

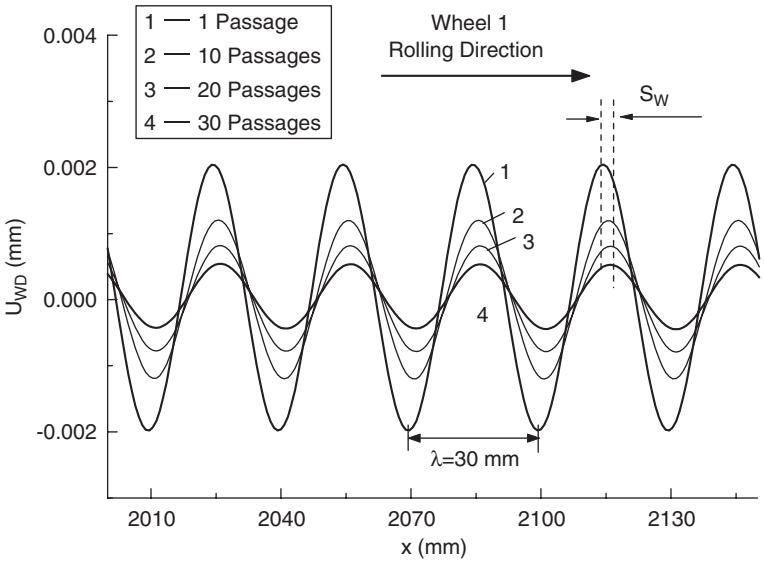

Fig. 19. Maximum undulatory wear caused by wheel 1.

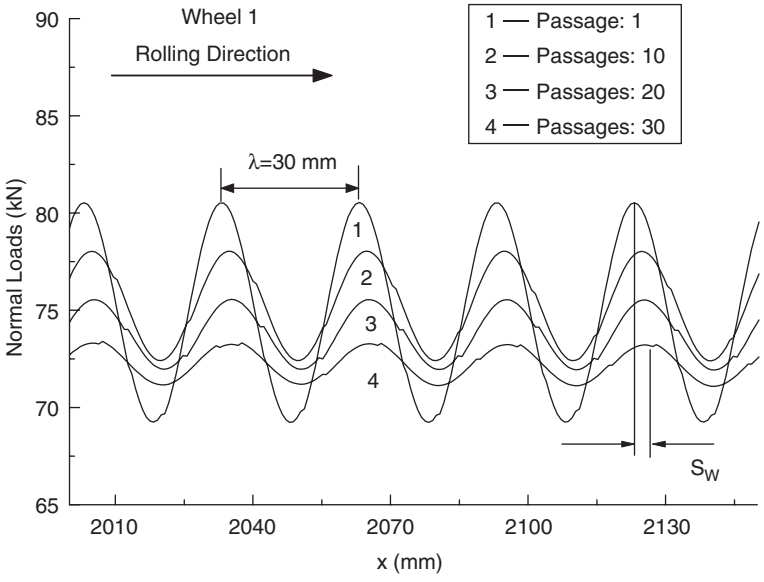

Fig. 20. Normal load of wheel 1 and high rail.

normal load is about 1/6 of that caused by the initial corrugation excitation. The phase of the normal load oscillation moves forward by about 4 mm, shown as S_w in Figs. 18 and 19.

Therefore, such a situation causes a moving of the new corrugation by about 4 mm after 30 passages. It should be noted that the movement of the initial corrugation in development is mainly caused by the phase difference between the initial corrugation excitation and the normal load without the other interfering factors. According to vibration theory, a system response always lags behind an excitation to the system in the time domain. The larger the wave-depth of the initial corrugation excitation is, the larger is the amplitude of the normal load fluctuation. However, the position where the maximum of the normal load fluctuation occurs differs from the trough of the initial corrugation. Therefore, the position of maximum depth of the new undulatory wear, for each passage, changes with the undulatory wear accumulating as the excitation. This is a reason why the initial corrugation in development has a tendency to move. The reason why the initial corrugation with a single wavelength decreases with increasing number of the train passages should be explained as, under an excitation of the initial corrugation with a single wavelength, the wheel and rail normal load fluctuates at a few frequencies (see Figs. 7 and 21). The passing frequencies of the new undulatory wear depend on the frequencies of the normal load fluctuations. In such a situation, the new accumulating undulatory wear gradually levels out the initial corrugation with a single wavelength with increasing number of the passages. Regarding this, Ref. [32] has a detailed discussion.

For the evolution of the initial corrugation with a fixed wavelength larger than 30 mm, the same situation occurs. So, the present numerical analysis brings about an interesting conclusion that the initial corrugation with a passing frequency (a fixed wavelength) does not develop with increasing number of the passenger car passages even though the passing frequency of the initial corrugation is the same as the natural frequency of the track. It is because that the track usually vibrates at a few frequencies under an action of the wheelset. During the passages, the vibration frequencies change probably, which depends on the extent (or energy) of the interaction between the wheel and the rail. Fig. 21 illustrates the linear spectra of the fluctuations of the normal loads of wheel 1 when the passages of the passenger car equal 1 and 30. For the first passage, the two peaks appear at $f_B = 740$ Hz and $f_C = 1485$ Hz on the solid line. It is clear that f_B is the frequency of the initial corrugation excitation. The peak value of the linear spectrum at f_B is much higher than that at its harmonic f_C. So f_B dominates the key wavelength of the new corrugation at the initial stage. After 30 passages, the peak at f_C disappears, the peak at f_B reduces, the normal load fluctuation goes up in the range less than 1600 Hz, and also another peak at $f_A \approx 38$ Hz appears, as shown by the solid line with circles in

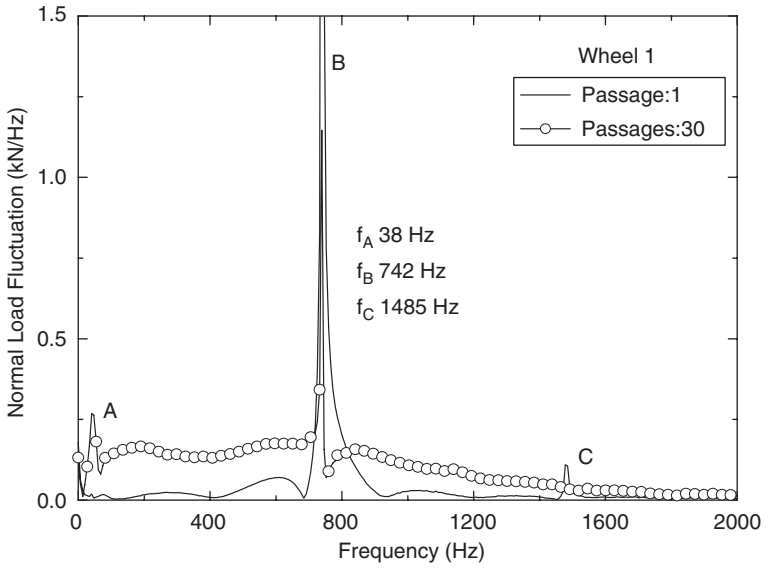

Fig. 21. Linear spectrum of normal load fluctuation.

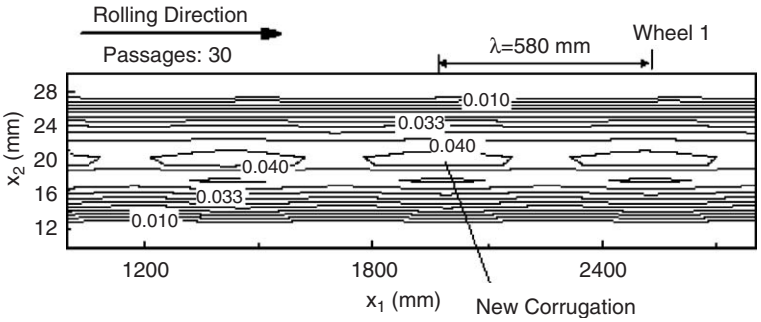

Fig. 22. Pattern of new wear with 580 mm wavelength and small depth.

Fig. 21. f_A is close to the sleeper passing frequency, as shown in Fig. 8. However, the peak value of the linear spectrum at f_B is much higher than that at f_A. So after 30 passages f_B still controls the key wavelength of the corrugation evolution. Due to a gradual increase of the normal load fluctuation at 38 Hz, a wavelength near 580 mm with very small wave-depth develops in the pattern of the new corrugation, as shown in Fig. 22, after 30 passages. It is noted that Figs. 22 and 18(c) stand for the same case. They were obtained by processing the data in different domain and contour levels. The wavelength about 580 mm is close to the sleeper pitch, 600 mm. The discrete sleeper supports probably cause such anundulatory wear with 580 mm wavelength. Whether the conclusion is correct is still an open question. This frequency will be further investigated by the authors.

After 30 passages, the evolutions of the initial corrugation on the rail under wheels 2, 3 and 4 are shown in Fig. 23. It is interesting that the initial corrugation in evolution on the low rail under wheel 2 has a tendency to move backward, as shown in Fig. 23(a), by about $S_w \approx 6$ mm. However, the evolution of the initial corrugation under an action of the trailing wheelset does not appear to have a tendency to move. In Ref. [32], the model of rail corrugation considered just a coupling of a single wheel and rail. A conclusion drawn from Ref. [32] is that the developing corrugation has a tendency to move forward. This conclusion is not general because the model in Ref. [32] ignored the across influences of the interactions of the rails and the four wheels of the same bogie. As we know, the movement of the developing corrugation can depress the growth of the corrugation. If the phase of developing corrugation does not change, the depth at its trough increases quickly with increasing number of the wheelset passages.

4. Conclusions

A three-dimensional train–track model for study of rail corrugation is put forward to analyse the effect of rail corrugation with different depths and wavelengths on the dynamic behaviour of a passenger car and a curved track in detail. Also the evolution of initial corrugation with different wavelengths is investigated. In numerical analysis, Kalker's non-Hertzian rolling contact theory is modified and used to calculate the frictional work density on the contact area of the wheel and rail in rolling contact. The rail material loss per unit area is assumed to be proportional to the frictional work density, which is used to determine the wear depth of the contact surfaces of the curved rails. The combined influences of the corrugation excitation and the vertical and lateral coupling dynamics of the passenger car and the curved track are taken into account. The numerical results obtained lead to the following conclusions:

(1) The corrugation with high passing frequencies has a great influence on the dynamic performance of the wheelset and track, but little on the car-body and the bogie frame.
(2) Under the condition of the same speed and the same wavelength, the deeper the corrugation depth from peak to trough is, the greater the influence on the dynamic performance and the rail material wear are. However, under the condition of the same speed and the same wave-depth, the longer the corrugation wavelength is, the smaller the influence and the wear are.

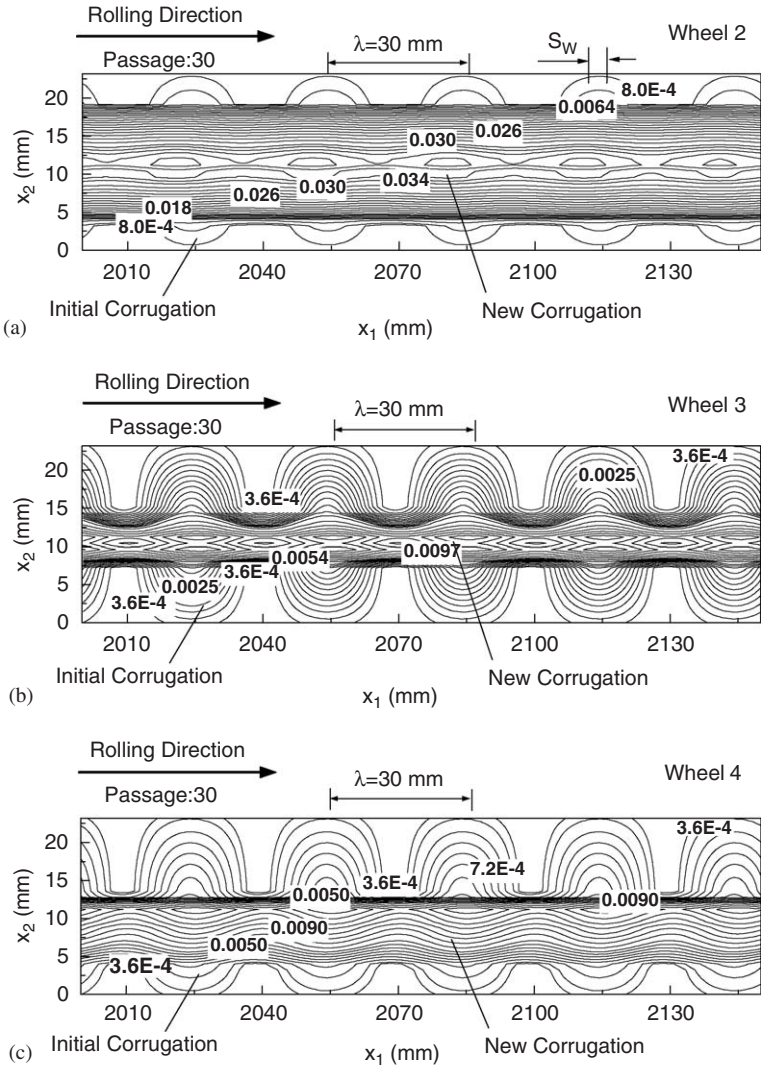

Fig. 23. Patterns of initial corrugation evolutions: (a) caused by wheel 2; (b) caused by wheel 3; (c) caused by wheel 4.

(3) The initial corrugation causes the vibration of the wheelsets and the track, such vibration contains a few natural frequencies of the track, which are easily excited when the passenger car passes over the corrugated rails. The new undulatory wear with a few different wavelengths levels out the initial corrugation gradually. The new undulatory wear for each passage gradually decreases with the gradual decreasing of the initial corrugation excitation. Therefore, the initial corrugation with a fixed wavelength on the rail running surface does not have a tendency to grow with increasing number of train passages. Its development depends on the track natural frequencies to be easily excited.

(4) The evolution of the initial corrugation caused by the leading wheelset has a tendency to move along the rail running surface.

(5) The track stiffness has, of course, a great influence on the initiation and development of rail corrugation and the wear. If we change any parameter of the track, such as the geometry size, the equivalent springs and dampers among parts of the track, the stiffness, the natural frequencies and the easily excited frequencies of the track can be changed. Therefore, this leads to the corrugation with different wavelength and wave-depth. These interesting phenomena will be further investigated by the authors.

Acknowledgements

This project is supported by National Natural Science Foundation of China (No. 59935100), Foundation of PhD Student Education Ministry of China (No. 20020613001) and FANEDD (No. 200248).

The authors are grateful to Professor David Thompson and Dr. Xiaozhen Sheng for their valuable technical advice.

References

[1] Y. Sato, A. Matsumoto, K. Knothe, Review on rail corrugation studies, *Wear* 253 (2002) 130–139.
[2] K. Knothe, B. Ripke, The effects of parameters of wheelset, track and running conditions on the growth rate of rail corrugation, *Vehicle System Dynamics* 18 (1989) 345–356.
[3] K. Hempelmann, F. Hiss, K. Knothe, B. Ripke, The formation of wear patterns on the tread, *Wear* 144 (1991) 179–195.
[4] K. Hempelmann, K. Knothe, An extended linear model for the prediction of short pitch corrugation, *Wear* 191 (1996) 161–169.
[5] J.J. Kalker, Considerations on rail corrugation, *Vehicle System Dynamics* 23 (1994) 3–28.
[6] J.B. Nielsen, A nonlinear wear model, ASME, *Rail Transportation* RTD-13 (1997) 7–20.
[7] J.B. Nielsen, Evolution of rail corrugation predicted with a nonlinear wear model, *Journal of Sound and Vibration* 227 (1999) 915–933.
[8] E. Tassilly, N. Vincent, A linear model for the corrugation of rails, *Journal of Sound and Vibration* 150 (1991) 25–45.
[9] R.A. Clark, P. Foster, On the mechanism of rail corrugation formation, in: *Proceedings of the Eighth IAVSD Symposium*, Swets and Zeitlinger, Amsterdam/Lisse, 1984, pp. 72–85.
[10] R.A. Clark, Slip–stick vibrations may hold the key to corrugation puzzle, *Railway Gazette International* 7 (1984) 531–533.
[11] R.A. Clark, G.A. Scott, W. Poole, Short wave corrugation-an explanation based on stick-slip vibrations, in: *Applied Mechanics Rail Transportation Symposium 96*, ASME, 1988, pp. 141–148.
[12] A. Böhmer, T. Klimpel, Plastic deformation of corrugated—a numerical approach using material data of rail steel, *Wear* 53 (2002) 150–161.
[13] X. Jin, Z. Wen, K. Wang, W. Zhang, Effect of a scratch on curved rail on initiation and evolution of rail corrugation, *Tribology International* 37 (2004) 385–394.
[14] A. Igeland, H. Ilias, Rail head corrugation growth predictions based on non-linear high frequency vehicle/track interaction, *Wear* 213 (1997) 90–97.
[15] C. Anderson, A. Johansson, Prediction of rail corrugation generated by three-dimensional wheel–rail interaction, *Wear* 257 (2004) 423–434.
[16] Y.Q. Sun, M. Dhanasekar, D. Roach, A three-dimensional model for the lateral and vertical dynamics of wagon-track systems, *IMechE Journal of Rail and Rapid Transit* 217 (F) (2003) 31–45.
[17] T.X. Wu, D.J. Thompson, An investigation into rail corrugation due to micro-slip under multiple wheel/rail interactions, *Wear* 258 (2005) 1115–1125.
[18] A. Matsumoto, Y. Sato, M. Nakata, M. Tanimoto, K. Qi, Wheel–rail contact mechanics at full scale on the test stand, *Wear* 191 (1996) 101–106.
[19] A. Matsumoto, Y. Sato, H. Ono, M. Tanimoto, Y. Oka, E. Miyauchi, Formation mechanism and countermeasures of rail corrugation on curved track, *Wear* 253 (2002) 178–184.
[20] Q.Y. Liu, B. Zhang, Z.R. Zhou, An experimental study of rail corrugation, *Wear* 255 (2003) 1121–1126.
[21] Y. Suda, H. Komine, T. Iwasa, Y. Terumichi, Experimental study on mechanism of rail corrugation using corrugation simulator, *Wear* 253 (2002) 162–171.
[22] S.L. Grassie, Corrugation: variations on an enigma, *Railway Gazette International* 146 (1990) 531–533.
[23] J. Kalousek, K.L. Johnson, An investigation of short pitch wheel and rail corrugation on the Vancouver mass transit system, *Proceedings of the Institution of Mechanical Engineers* 206 (1992) 127–135.
[24] S.L. Grassie, J. Kalousek, Rail corrugation: characteristics, cause and treatments, *Proceedings of the Institution of Mechanical Engineers* 207 (Part F) (1993) 57–68.
[25] M. Ishida, T. Moto, M. Takikawa, The effect of lateral creepage force on rail corrugation on low rail at sharp curves, *Wear* 253 (2002) 172–177.
[26] Y. Suda, M. Hanawa, M. Okumura, T. Iwasa, Study on rail corrugation in sharp curves of commuter line, *Wear* 253 (2002) 193–198.
[27] E.G. Vadillo, J.A. Tarrago, G.G. Zubiaurre, C.A. Duque, Effect of sleeper distance on rail corrugation, *Wear* 217 (1998) 140–146.
[28] W.M. Zhai, C.B. Cai, S.Z. Guo, Coupling model of vertical and lateral vehicle/track interactions, *Vehicle System Dynamics* 26 (1996) 61–79.
[29] Z.Y. Shen, J.K. Hedrick, J.A. Elkins, A comparison of alternative creep-force models for rail vehicle dynamic analysis, in: *Proceedings of the Eighth IAVSD Symposium*, Cambridge, MA, USA, 1983, pp. 591–605.
[30] W.M. Zhai, Two simple fast integration methods for large-scale dynamic problems in engineering, *International Journal for Numerical Methods in Engineering* 39 (1996) 4199–4214.

[31] W.M. Zhai, *Coupling Dynamics of Vehicle-Track*, China Railway Press, Beijing, 2001 (in Chinese).
[32] X.S. Jin, Z.F. Wen, K.Y. Wang, Effect of track irregularities on initiation and evolution of rail corrugation, *Journal of Sound and Vibration* 285 (2005) 121–148.
[33] J.J. Kalker, A fast algorithm for the simplified theory of rolling contact, *Vehicle System Dynamics* 11 (1) (1982) 1–13.
[34] J.J. Kalker, *Three-Dimensional Elastic Bodies in Rolling Contact*, Kluwer Academic Publishers, The Netherlands, 1990.
[35] P.J. Bolton, P. Clayton, I.J. McEwan, Rolling-sliding wear damage in rail and tyre steels, *Wear* 120 (1987) 145–165.
[36] P. Clayton, Tribological aspects of wheel–rail contact: a review of recent experimental research, *Wear* 191 (1996) 170–183.